POLITECNICO DI MILANO

Ingegneria dei Sistemi
Corso di Laurea in Ingegneria Biomedica

Fluid-structure interaction simulations of hemodynamics in mice: applications to hypertension research

Relatore:
Prof. Francesco Migliavacca

Correlatore:
Prof. C. Alberto Figueroa

Candidata:
Federica Cuomo
765319

Anno Accademico 2012-2013

Contents

List of Figures

List of Tables

Abstract

Motivation

Arterial stiffening is both cause and consequence of hypertension,currently the main cause of death in Europe. Hemodynamic metrics such as central pulse pressure (cPP) and pulse wave velocity, which can be non invasively measured, are now known as important predictive factors of diseases and diseases susceptibility. Computational Fluid Dymanic techniques enable an accurate representation of hemodynamics in the central arteries, hence providing a non-invasive estimate of the time varying pressure and flow. These techniques, combined with experimental and imaging data are fundamental in understanding the correlation between arterial stiffness and hemodynamics. Computational simulations can provide improved interpretations of clinically measurable metrics of pulse wave velocity and even identify new metrics based on pressure waveform analysis. The objective of this work is to validate a new computational biomechanical fluid-solid interaction tool in a mouse model. This tool employs a Fluid Structure Interaction (FSI) technique to represent the deformability of the wall vessel which is fundamental to capture pulse pressure propagation. It also uses a multi-domain method to include the impact of distal vasculatures in the aortic geometry, as it well known that distal vessels have a remarkable influence on the hemodynamics of the central arteries.

Methods

We set out to search reliable flow, pressure and geometrical data in mice to use both as input data and as results validation. In vivo measurements in mice are challenging due to the small dimension of the body and the fast

heart rate. The data used in the simulations have been carefully chosen to ensure consistency between weight, age and strain of the mice tested. Considering this, we found references for flow data in ascending aorta, left common carotid, innominate artery and infra-renal abdominal artery; systolic, diastolic and mean pressure values in the aortic arch; and vessel diameter dimensions for three locations along the aorta and for renal, mesenteric, celiac, left common carotid, subclavian and innominate arteries. An initial 3-D geometrical model was built from micro-CT imaging of a vascular casting using the custom software Simvascular. The model included ascending, descending and abdominal aorta plus significant segments of subclavians, carotids, renal arteries, mesenteric, celiac and tail. The vascular casting technique, performed at Biomedical Department of Yale University, resulted in geometry with smaller than physiological diameters. This geometry resulted in highly unrealistic pressures when pulsing physiological levels of flow, due to the artificially large resistance of the model. Therefore the initial geometry was upscaled to match the diameter data found in literature. The initial model did not represent the intercostal vessels, as they are too narrow to be captured by either imaging. Since these vessels carry a significant amount of flow, nine pairs of intercostal arteries were added along the thoracic aorta of the model.

Once the model was ready, a finite element mesh was obtained in Simvascular and a first simulation was run with rigid walls; followed by a gradient-based mesh adaptivity technique. This technique took into account the distribution of velocity gradients of the previous simulation to obtain a uniform distribution of the error in all special directions.

The computational fluid dynamics method used relies on a multi-scale modeling approach, whereby a decomposition of the spatial domain and of the variables is introduced. Within this approach two domains coexist: a numerical domain in which the Navier-Stokes equations for an incompressible Newtonian fluid are solved and an analytic domain in which a lumped parameter formulation is employed. In our case the numerical domain was the 3-D geometrical model of the central arteries and the major branches, while the three-elements Windkessel models were adopted to represent the distal ves-

sels until the capillaries level. The Windkessel model is an electrical circuite analogue of the circulation: it consists of a proximal resistance connected in series with a parallel of a distal resistance and a compliance. Onece a three-element Windkessel model is coupled at each outlet of the 3-D domain, a model with large number of vessels, as ours, requires the specification of numerous parameters. A systematic approach to obtain the parameters based on 1D-theory [15], was adopted in this work. Briefly, the total resistance of the model (combination of 3-D and 0-D) was calculated by taking into account the mean value of the flow at the inlet and target mean pressure. The resistance of the 3-D geometry was then assumed to be zero, since the contribution of the central arteries to the total resistance is much smaller than that of the distal circulation. The total resistance for each outlets was split between proximal and distal resistances. The proximal resistance was calculated to match the characteristic impedance of the correspondent outlet of the upstream domain. A similar approach was adopted to evaluate the compliance values: a total arterial compliance was first calculated. Unlike with the resistance, the contribution of the central arteries to the total arterial compliance can not be assumed equal to zero. We thus estimated the compliance of the central arteries as the sum of the compliance of each vessel. Lastly, the peripheral compliance which was then distributed among the different outlets in proportion to the flow distribution.

The computational fluid dynamic method adopted in this work also includes a fluid-structure interaction technique. This aspect is fundamental in order to capture pulse pressure propagation in the contest of arterial stiffening and hypertension. The FSI "Coupled Momentum" method developed by Figueroa and Taylor at Stanford was used [16]. Here, the elastodynamic equations representing the deformation of the wall are incorporated in the stabilized finite element formulation of the Navier-Stokes equations and a traction field describing the wall behavior is applied as boundary condition to the lateral boundary of the fluid domain. The vessel wall is modeled as a linear elastic membrane characterized by a young modulus E, a Poisson ratio $\nu = 0.5$, and a thickness h. Variable tissue properties were considered in this thesis. The thickness h was estimated as 10% of the local radius according to literature

data [1]. Experimental stiffness values were obtained at the Department of Biomedical Engineering of Yale University. Stiffness data measured at four different locations were interpolated throughout the model. The support of the perivascular tissue and other organs on the vessels was also modeled as a traction acting on the outer boundary of the arterial wall.

Results

Four simulations were performed: a baseline case, a case with reduced distal compliance values and two cases with increased vessel stiffness in the central vessel. A representative ascending aortic flow waveform acquired from Lujan et al. [2] was prescribed. The average cardiac output was 11.92 ml/min and the cardiac cycle 0.147 s. The flow distribution obtained in the baseline case was in good agreement with literature data [3] [4], even though there are some qualitative differences in the shape of the waveforms (see Figure 1). This incongruity is probably due to the lack of diastolic backflow in the ascending aorta flow data considered[3]; and also ndue to the need for further tunning of the outflow boundary condition parameters. On the other hand the shape and range of the pressure waveform correspond well to the known physiological behavior [17]. As reported in literature, no pulse pressure amplification along the aorta is observed in mice. This is in contrast with what happens in young humans. The pressure in the ascending aorta ranged from 93 to 120 mmHg, while in the infra-renal abdominal aorta the range was 93 to 113 mmHg (see Figure 1). In the interest of investigating whether the amplification of the pulse is obtainable in mice geometry, the RCR values of the baseline case were modified by decreasing the compliance of the lower vessels. Under these conditions, augmentation of the pulse pressure down the aorta was obtained. The effects of augmented arterial stiffness due to aging and hypertension were also examined. Two simulations were set up with adifferent distributions of elastic modulus E (increased by a factor of 2 and 3 relative to the baseline, respectively). In both cases, the pulse pressure and pulse wave velocity increased along the aorta with higher stiffness as reported in literature [6].

Discussion

The most important limitation of this work is the uncertainty and multiple origins of the data utilized. A big percentage of the work researching literature data on vessels diameters. Similarly, pressure data at different locations were reported in different papers, making it difficult to have consistent experimental conditions. Lastly, the tissue properties were measured at four locations only. Future work will involve considering the full biaxial experimental data of the vessel stiffness rather than just the circumferential component and the use of a lumped-parameter heart model to couple the left ventricle and the arterial network. The innovation of this work is the reproduction of physiological pressure waveforms and flow distribution in a realistic model of the mouse vasculature.

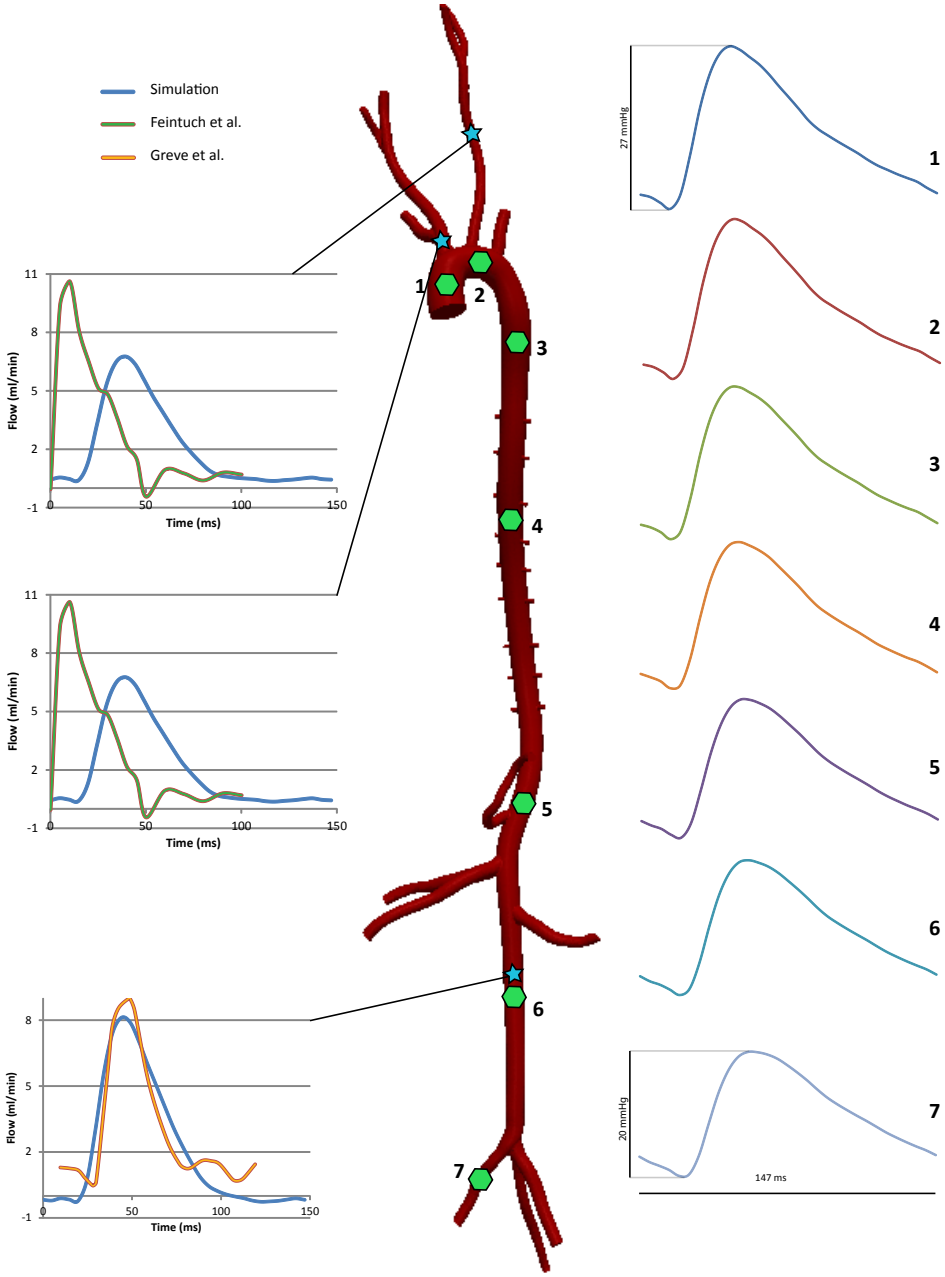

Figure 1: Pressure simulation at seven different location along the aorta and flow waveforms compared to literature data at representative locations.

Sommario

Introduzione

Le malattie cardiovascolari sono la principale causa di morte in Europa. L'irrigidamento delle arterie é oggigiorno riconsciuto come causa e conseguenza dell'ipertensione che é uno dei principali fattori di rischio per le malattie cardiovascolari. Il polso pressorio e la sua velocitá sono misurabili tramite procedure non invasive e sono ritenuti importanti fattori predittivi di eventi cardiovascolari. Vi é necessitá di capire come i cambiamenti della rigidezza arteriosa influenzino localmente e globalmente l'emodinamica. In questo contesto diventano sempre piu' importanti gli studi computazionali che permettono una riproduzione accurata e realistica di grandezze emodinamiche, fornendo una stima accurata e non invasiva dell'onda pressoria. L'obiettivo di questo lavoro é validare un nuovo strumento di biomeccanica computazionale della anatomia del topo. Un metodo d'interazione fluido-struttura é stato utilizzato per includere la deformabilitá delle pareti dei vasi nell'analisi della propagazione del polso pressorio. Un approccio multi-scala é stato applicato per includere i vasi distali, fino a livello dei capillari, nel modello siccome la rete arteriosa distale ha una forte influenza sull'emodinamica delle arterie centrali.

Metodi

Una componente molto importante del lavoro é stata la ricerca in letteratura di dati affidabili riguardanti il flusso sanguigno, la pressione e le dimensioni dei vasi nei topi. Le misurazioni in vivo sono rese difficili dalle ridotti dimensioni dell'anatomia e dall'alta frequenza cardica (circa 600bpm) di questi animali. I dati sono stati attentamente scelti, essendo a conoscenza dei

limiti e dei vantaggi delle tecnologie attualmente in uso e mantenedo coerenza tra il peso, l'etá e la tipologia del topo. Le grandezze di riferimento prese in considerazione sono: la **variazione del flusso nel tempo** nell'aorta ascendente, nell'arteria carotidea comune, innominata, e nell'aorta addominale sottorenale, i valori di **pressione media, sistolica e diastolica** misurati nell'arco aortico ed il **diametro** dell'aorta (3 diverse posizioni), dell'arteria renale, mesenterica, celiaca, carotidea comune, succlavia e innominata.
Dalle immagini micro-CT di un campione ottenuto tramite la tecnica di vascular corrosion casting é stato costruito il modello geometrico tridimensionale utilizzando il software Simvascular. La procedura di corrosion casting é stata eseguita nel dipartimento di Biomedica dell'Universitá di Yale. Poiché il modello risultante sottostimava la geometria reale, i valori di pressione stimati dalle simulazioni risultavano maggiori di quelli fisiologici. Per questo motivo le dimensioni del modello geometrico sono state aumentate per riprodurre i valori dei diametri trovati in letteratura. Il modello originale comprendeva l'aorta ascendente, discendente e addominale oltre a segmenti delle arterie succlavia, carotidee, renali, mesenterica, celiaca e l'arteria della coda. Il modello originale non considerava le arterie intercostali, troppo piccole per poter essere visualizzate nelle immagini. Poiché in questi vasi scorre una parte importante della gittata cardiaca, nove paia di arterie intercostali sono state aggiunte alla geometria lungo l'aorta toracica.
La mesh del modello é stata ottenuta usando la libreria di Simvascular ed una prima simulazione con pareti rigide é stata eseguita ed in base ai risultati la mesh é stata adattata tenendo in considerazione la distribuzione del gradiente di velocitá, per ottenere una distribuzione uniforme in tutte le direzioni.
Al fine di eseguire diversi livelli di modellizazione, é stata utilizzato un approccio multi-scala che comprende una decomposizione del dominio e delle variabili. L'approccio multi-scala suddivide il dominio in un dominio numerico, in cui vengono risolte le equazioni di Navier-Stokes per un fluido newtoniano incomprimibile, ed un dominio analitico, in cui viene adottata una formulazione a parametri concentrati. Nel nostro caso, il modello tridimensionale delle arterie centrali e delle prinicpali diramazioni é il dominio numerico, mentre un modello Windkessel a tre elementi é stato impiegato

come dominio analitico per rappresentare i vasi distali fino a livello dei capillari. Il modello Windkessel é un analogo elettrico della circolazione sanguigna costituito da una resistenza prossimale in serie al parallelo di una resistenza distale ed un condensatore (RCR). Un modello Windkessl a tre elementi é accoppiato ad ogni vaso del modello tridimensionale; una geometria complessa con un numero elevato di diramazioni richiede quindi la specificazione di molti parametri. In questo lavoro é stato adottato un approccio basato sulla teoria 1-D [15] per ottenere i valori di questi parametri in modo sistematico. Brevemente, una resistenza assegnata a tutto il modello (combinazione della parte 3-D e della parte 1-D) é stata calcolata considerando il valore medio del flusso prescritto a livello dell'aorta ascendente e la pressione media desiderata. La resistenza rappresentata dal modello 3-D é stata considerata nulla, poiché il contributo delle arterie centrali é decisamente inferiore rispetto alla componente distale. La resistanza totale é stata quindi partizionata tra le resistanze prossimali e distali di ogni modello Windkessel. La resistenza prossimale del modello Windkessel é stata calcolata come impedenza caratteristica dell'estremitá del vaso corrispondente. Un approccio simile é stato adottato per valutare i valori delle capacitá; una capacitá totale é stata calcolata, ma in questo caso il contributo delle arterie centrali non puó essere assunto nullo. La capacitá del modello 3-D é quindi stata calcolata come somma delle capacitá di ogni arteria. Da questi due valori é stato possibile ricavare la capacitá periferica che é stata poi distribuita tra i diversi vasi proporzionalmente alla distribuzione del flusso.

Per poter rappresentare la propagazione del polso pressorio, che é strettamente collegata alla rigidezza arteriosa e all'ipertensione, si é utilizzata una tecnica d'interazione fluido-struttura (FSI). In particolare, si é utilizzato il metodo FSI "Couplde momentum" sviluppato da Figueroa e Taylor all'Universitá di Stanford [16]. Le equazioni dell'elastodinamica rappresentanti la deformazioni della parete del vaso sono state incorporate nella formulazione agli elementi finiti delle equazioni di Navier-Stokes e un vettore di trazione originato dall'interazione fluido-struttura é stato appplicato come condizione al contorno al dominio fluido. La parete arteriosa é stata modellizzata come una membrana elastica lineare caraterrizzata da un modulo di

Young E, un modulo di Poisson $\nu = 0.5$ e uno spessore h. Le proprietá meccaniche della parete sono state considerate variabili in tutto il modello. Lo spessore della parete h é stato specificato come il 10% del raggio corrispondente, in accordo con quanto riportato in letteratura [1]. I valori sperimentali di rigidezza sono stati forniti dal dipartimento di Ingegneria Biomedica dell'universitá di Yale. I dati rilevati in quattro diverse posizioni sono stati interpolati lungo tutto il modello. Il sostegno dei vasi da parte dei tessuti perivascolari e degli organi é stato rappresentato come una condizione al contorno di trazione all'esterno della parete arteriosa.

Risultati

Sono state effettuate quattro simulazioni: un caso base, un caso con valori delle capacitá periferiche ridotte e due casi con rigidezza della parete del vaso aumentata a livello delle arterie centrali. Un valore di flusso variabile nel tempo, tipico dell'aorta ascendente [2], é stato utilizzato. Il valore della gittata cardiaca era di 11.92 ml/min e della durata del ciclo cardiaco di 0.147s. La distribuzione della portata ottenuta nel caso base é in buon accordo con i valori riportati in letteratura [3] [4], ma la forma dell'onda é qualitativamente diversa (Figura 2). Questa incongruenza é probabilmente dovuta alla differenza di forma d'onda nell'aorta ascendente riportata dall'articolo usato come riferimento [3] e potrá essere migliorata in futuro aggiustando iterativamente i parametri RCR. La forma e la variazione dell'onda pressoria, invece, corrispondono al comportamento fisiologico standard [17]. Come riportato in letteratura, l'ampilificazione del polso pressorio lungo l'aorta non si osserva nei topi, al contrario di cio' che avviene nell'uomo adulto. La pressione nell'aorta ascendente varia tra 93 e 120 mmHg e nell'aorta addominale sottorenale tra 93 e 113 mmHg (Figura 2). Per investigare se l'amplificazione del polso pressorio é ottenibile nella geometria del topo, i valori RCR del caso base sono stati modificati diminuendo le capacitá dei vasi inferiori. Con queste condizioni si é ottenuto l'aumento del polso pressorio. Infine sono stati esaminati gli effetti dell'irrigidimento arteriale causato dall'invecchiamento. A questo scopo sono state effettuate due simulazioni con diversa distribuzione del modulo elasitco E, aumentato di un fattore 2 e 3, rispettivamente. In

entrambi i casi, il polso pressorio e la velocitá dell'onda aumentano lungo l'aorta come riportato in letteratura [6].

Discussione

Le principali limitazioni del lavoro svolto sono causate dai limiti delle attuali tecnologie per l'acquisizione delle grandezze misurate nei topi e la divrase origine dei dati utilizzati. Una parte fondamentale del lavoro é stata la ricerca in letteratura delle dimensioni dei diametri arteriali. I valori pressori in diverse posizioni dell'albero arterioso sono riportati da fonti diversi, rendendo difficile avere condizioni sperimentali coerenti per poter validare la distruibuzione di pressione del modello. In ultimo, le proprietá meccaniche dei tessuti sono state misurate solo in quattro posizioni.
In uno sviluppo futuro si considererá l'utilizzo di tutti i dati sperimentali biassiali della rigidezza della parete piuttusto che solo la componente circonferenziale, oltre all'uso di un modello di cuore a parametri concentrati per accoppiare il ventricolo sinistro e la rete arteriale. Il contributo principale di questo lavoro é la riproduzione di una forma d'onda pressoria fisiologica ed una corretta distriuzione della portata in un modello realistico della rete vascolare dei topi.

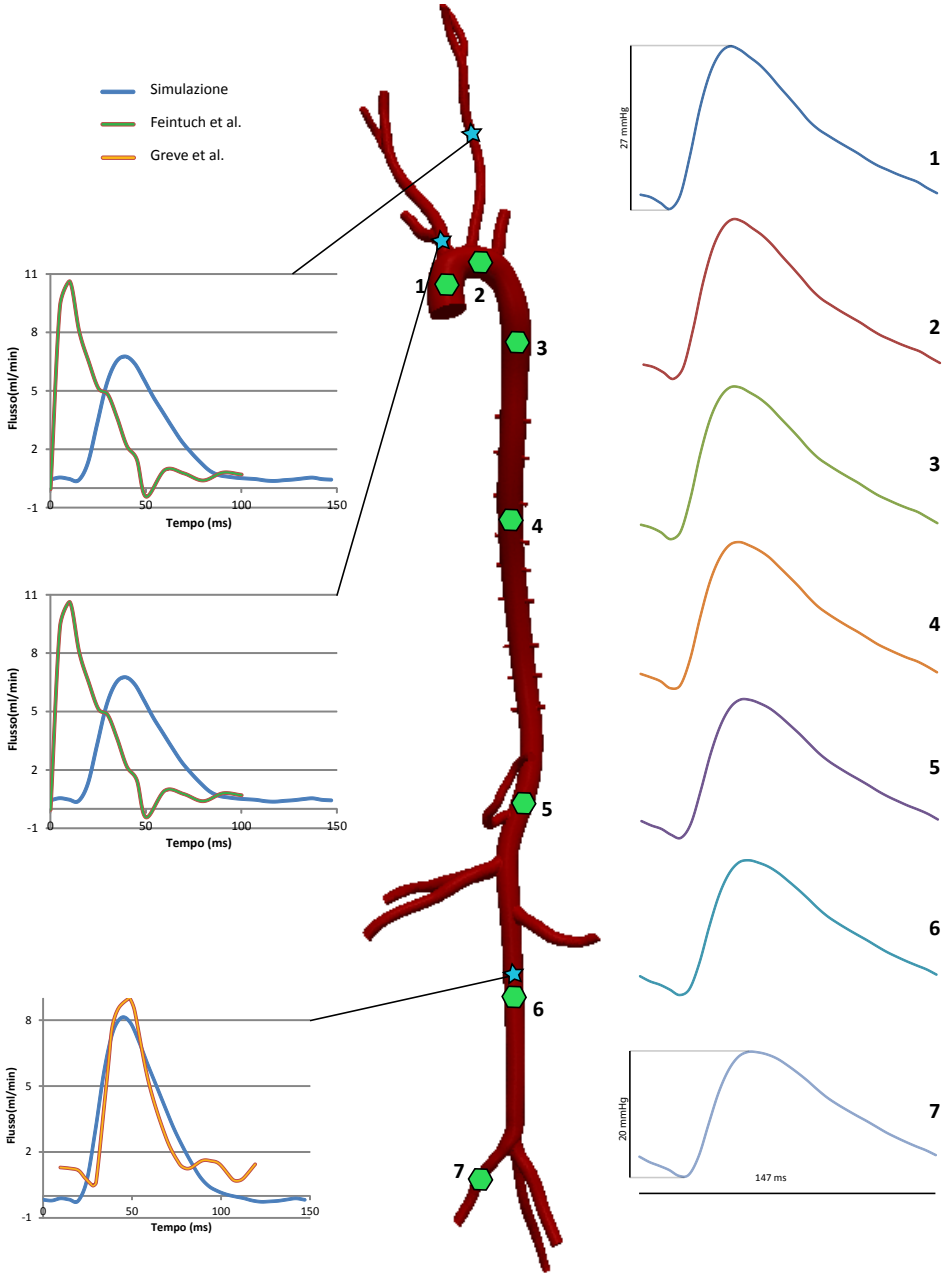

Figure 2: Pressione risultante in sette diverse posizioni lungo l'aorta e onde di flusso in posizioni rappresentative confrontato ai dati riportati in litteratura.

Chapter 1

Introduction

1.1 Clinical motivation

Cardiovascular disease (CVD) is the main cause of death in Europe, accounting for more deaths than cancer and trauma combined: CVD represents 47% of all deaths in Europe (approximately 4 millions per year) [18].
Hypertension is one of the main risk factors in CVD. Arterial stiffness of the central arteries is now recognized as both a cause and a consequence of hypertension. Hemodynamics metrics such as central pulse pressure (cPP) and carotid to femoral pulse wave velocity (CFP) have become important clinical indicators of disease and disease susceptibility.

In young healthy subjects the pressure wave exhibits an increase in amplitude traveling down the aorta. This is due to the increase in stiffness of the vessel wall with increasing distance from the heart. In older subjects, the vessels are stiffer and this results in increased amplitude of the pressure waves, although the amplification factor between central locations and distal locations is smaller (see Figure 1.1). Therefore in elderly subjects the pressure wave in the ascending aorta is similar to the pressure wave recorded in the iliac artery [1]. Furthermore the pulse wave velocity (PWV) is smallest in the ascending aorta where the vessel wall is the most compliant, and reaches a maximum value in the stiffer abdominal aorta before declining again at the iliac bifurcation level. Arterial stiffening in normal aging or disease results

in increased PWV values in the central arteries. This is due to the fact that reflected pressure waves from the peripheral circulation arrive earlier at the ascending aorta and they constructively interfere with the incident waves [19]. The augmentation index (AIx) is a metric that quantifies the increase in pulse pressure due to wave reflection and is commonly used as a surrogate for arterial stiffness.

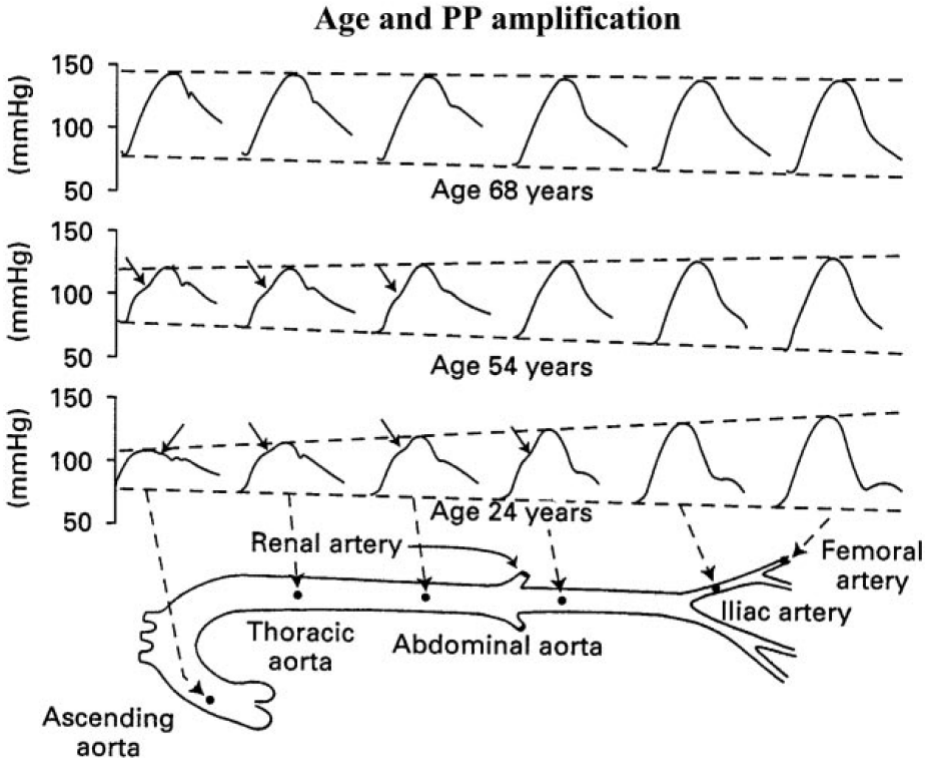

Figure 1.1: Propagation of the pulse pressure (PP) wave from central to peripheral arteries in adult humans aged 24, 54 and 68 years. [1]

Changes in vessels wall mechanics may progress both spatially (from proximal to distal vessels [20]) and temporally (via biological aging, not just chronological aging [19],[21]). Hence, there is a need to understand how local changes in arterial stiffness can affect local and global hemodynamics. In addition it appears that the change in amplitude of the hemodynamic loading (i.e., the pressure) over the cardiac cycle is fundamental to mechanobiological

responses of the arterial wall. Computational studies provide a powerful tool to investigate this problem, as they make it possible to represent information in the 3-D flow field with high temporal and spatial resolution, providing accurate and non-invasive estimates of pressure waveforms. This is important since even though it is possible to measure pulsatile flow in vessels non invasevely using Doppler, it is not possible to measure non invasively the time varying pressure within most arteries. Hence, computational studies can be used to relate hemodynamic changes (i.e., changes in pressure) and mechanobiological responses (i.e., arterial stiffening and thickening).

1.2 The big picture

This work is framed within a larger research project that combines animal models, computational solid mechanics and computational fluid dynamics to investigate the onset and evolution of hypertension. The working hypothesis of the project is that loss of structural integrity of elastin fibers leads to changes in overall arterial stiffness that give rise to diverse vascular pathologies [21]. The project will exploit two mouse models of altered elastin-associated microfibrils that normally help organize and stabilize elastic fibers (fibrillin-1 and fibulin-5). These models develop hypertension naturally and often exhibit arterial complications including aortic dilatation, tortuosity, dissection and rupture. Moreover, it will be pharmacologically investigated, in the same mouse models, the effects of other alterations associated with hypertension such as the vasoactive dysfunction of endothelium, decreased proteolytic activity and reduced cross-linking of fibrillar collagen [22].

The first specific aim of the research project is to identify molecular and cellular mechanism of increased arterial stiffness that precede the development of hypertension in mouse models of altered elastin integrity, endothelial function, matrix metalloproteinase activity, and collagen cross-links. Specifically, we will quantify spatially and temporally progressive changes in large artery mechanics and hemodynamics.

The second specific aim of the project is to develop, verify and validate a novel computational biomechanical fluid-solid interaction tool using mouse

data. This will enhance the understanding of hemodynamic changes associated with spatial and temporal increases in central artery stiffness. The successful completion of this aim will provide improved interpretations of current clinically measurable metrics such as PWV and it will identify new metrics based on pressure waveform analysis.

The contribution of this thesis is inserted in the second specific aim: the objective of this work is to perform fluid structure interaction simulations in geometric models built from mouse image data to obtain realistic flow and pressure waveforms.
In the following section we describe the basics of the multiscale computational fluid dynamics framework used in this work.

1.3 Computational Fluid Dynamics framework

In order to produce realistic simulations of blood flow and pressure, the following elements are required:

- an appropriate geometry
- adequate boundary conditions

Regarding the geometry, a 3-D model of the central arteries and the main branches is necessary to represent the complex geometry of the arteries. A representation of the distal vessels is also important as they have an effect on the hemodynamics in the central arteries. The size and complexity of the distal circulation precludes a three-dimensional representation of the entire circuit and therefore the role of the distal vessels is represented by adequate outflow boundary conditions. The boundaries of a vascular model, no matter how geometrically complex it is, can be classified into three groups (see Figure 1.2):

- An inflow boundary Γ_g. In this face of the model a flow wave form is prescribed.
- A vessel wall boundary Γ_s. This boundary represents the interface between the fluid domain and the vessel wall. Different conditions are

applied depending on whether a rigid or deformable wall assumption is considered.

- An outflow boundary Γ_h. A weak pressure obtained via coupling with a RCR lumped parameters condition is used in order to represent the distal vasculature.

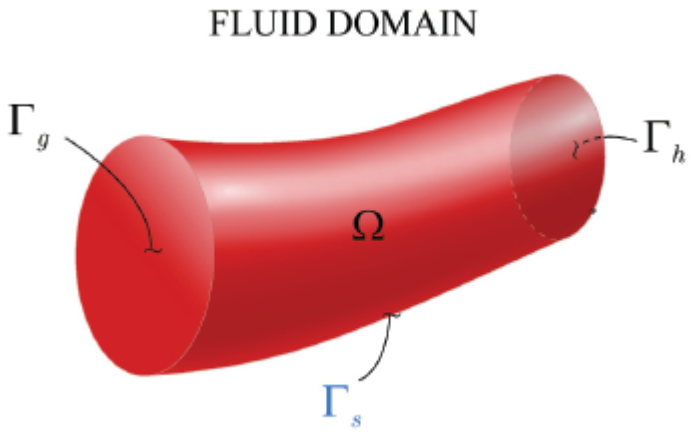

Figure 1.2: Tipical boundaries of a fluid domain in hemodynamics

To set up the fluid dynamic simulation, precise information on mice hemodynamics and geometry is necessary; this information should be preferentially measured in vivo. The small dimensions and fast heart rate (∼600 bpm) complicate the acquisition of necessary data and this lack of knowledge makes harder the validation of the model.

In the interest of investigating pressure waveforms and their role in arterial stiffening is important to capture pulse pressure propagation. For this purpose, it is mandatory to account for the deformability of the wall vessel using fluid structure interaction (FSI) techniques. FSI methods have been applied to patient-specific models of the thoracic aorta; where good agreement between simulated and observed vessel motion and hemodynamics was obtained [23]. However simulation of pulse wave velocity and pressure propagation has not been validated in a mouse model yet.

1.3.1 Outflow boundary conditions

Outflow boundary conditions are a critical component of the mathematical model. The choice of outflow boundary conditions was a significant influence in 3-D simulations of blood flow, as they represent the peripheral vasculature which strongly affects velocity and pressure fields in the 3-D domain.

In numerous fluid dynamic computations, prescribed velocity or pressure outflow boundary conditions have been considered [24], [13]. This approach, however, is inappropriate to model wave propagation phenomena. A slightly more sophisticated approach for boundary condition specification is the concept of resistance ($R = \frac{P}{Q}$). This boundary condition does not require the specification of either flow or pressure at the outlet. However this approach strongly affects wave propagation phenomena as it forces flow and pressure waves to be in phase and it produces non physiologic pressures in the case of flow reversal [25]. In this work a coupled 3D-0D approach presented in Figueroa et al. [16] and Vignon-Clementel [26] has been used. Lumped parameter models are coupled to the 3-D equations of blood flow and vessel wall dynamics. In these models, the parameters are assumed to be uniform in each spatial compartment and their behavior is described by a set of ordinary differential equations. The specific lumped parameter model used is a 3 element Windkessel model composed by a proximal resistance connected in series with a parallel of distal resistance and compliance (see Figure 1.3). An explicit relationship of pressure as a function of flow rate or velocity can be derived at the coupling interface.

The use of Windkessl models as outflow boundary condition in complex models with large number of vessels requires the specification of numerous parameters. In this work a systematic approach to obtain these RCR parameters based on 1D-theory is considered [15].

There have been a few computational simulations of hemodynamics in mice models. Huo et al. [24] investigated the distribution of hemodynamic parameters in the mouse aorta and primary branches. They prescribed pressure outflow boundary conditions (i.e, no reduced-order lumped parameter model). Simplifications were made for the vessel geometry (assumed cylin-

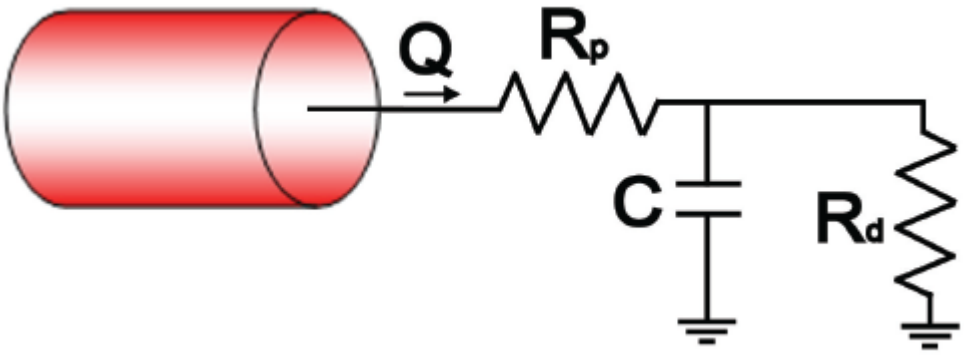

Figure 1.3: Three-element Windkessel model

drical) and a rigid assumption was considered for the wall. Pressure results were not reported.

Trachet et al. [13] computed hemodynamics in mouse-specific models. Time-dependent outflow velocity curves were imposed at the outlets and pressure results were not reported.

This work wants to illustrate the importance of using complex model geometry, fluid structure interaction techniques and adequate outflow boundaries conditions to obtain physiologic pressure wave forms in mouse models.

Chapter 2

Methods

In this chapter, we provide an overview of the data available in the literature on vascular geometry, flow and pressure, and mechanical properties. We then describe the specific steps taken to produce one mouse-specific geometry. We finish the chapter with a description the Computational Fluid Dynamics framework used in this work.

2.1 Data research in literature

Hemodynamic, geometrical and mechanical mice data allow to set up the computational simulations with adequate boundary conditions and to validate the results against the in vivo measurements. The fast heart rate (in the order of 600 beats/min) makes it difficult to use contrast agents for enhanced imaging in mouse. When building a geometric model of the mouse vasculature, it is important to pay attention to weight, age and strain of the mice tested, since the results are strongly depending on these factors.

2.1.1 Flow data

Reliable in vivo flow waveform measurements are important both for adequate inflow boundary condition at the level of ascending aorta, and also to validate the results. Lujan et al. [2] describe for the first time the use of an intact, conscious, and unrestrained mouse model of myocardial

ischemia/reperfusion and infarction. A 1.6-mm Silastic-type Doppler ultrasonic flow probe was permanently implanted on the ascending aorta and an occluder on the coronary artery. Measurements of ascending aortic blood flow were recorded in conscious mice, at rest and during exercise, before and during coronary artery occlusion, reperfusion and infarction. This model provides data free of the influence of anaesthetics, surgical trauma and restraint stress. The procedures were done in 16 male C57BL/6 mice 3 to 4 months of age with body weight 25-30g. The measurements were taken ten days after surgery. The paper reports the plot of ascending aorta flow recorded in control mice for six cardiac cycles together with the ECG tracing (see Figure 2.1). Since the recorded flow signal is not periodic; an average signal was calculated to use in the simulation. The ECG peaks were used to determine the starting point of each cycle. Each cycle was normalized in time and amplitude. This operation lead to a flow waveform with a Q_{mean} of 11.92 ml/min (see Figure 2.2).

Feintuch et al. [3] studied hemodynamics in the mouse aorta using a combination of Doppler ultrasound, MRI measurements, and numerical modelling. Eight inbred C57BL/6 adult mice were studied with Doppler ultrasound imaging: 4 males and 4 females, 20–25 g body weight. The animals were anesthetized with 1.5% isoflurane through a face mask. Blood flow velocity was measured at the mid level of the ascending aorta and proximal innominate artery, left common carotid artery, and left subclavian artery. Blood flow patterns were also measured using MRI in five inbred C57BL/6 mice: 3 males and 2 females, 20–25 g body mass. The mice were anesthetized for the scan duration with a mixture of 1.6% isoflurane gas and oxygen. Flow data was recorded in the ascending aorta, innominate artery and left carotid (see Figure 2.3). The measurements revealed a difference in total blood volume obtained with Doppler ultrasound and MRI. The Doppler ultrasound tends to overestimate the flow because it measures blood velocity in the centre of the vessel, which is multiplied by the vessel cross-sectional area to get flow. Since the ascending aortic flow is comparable to that reported by Lujan article, innominate artery and left carotid flow data will be used to validate the flow output obtained by the simulations.

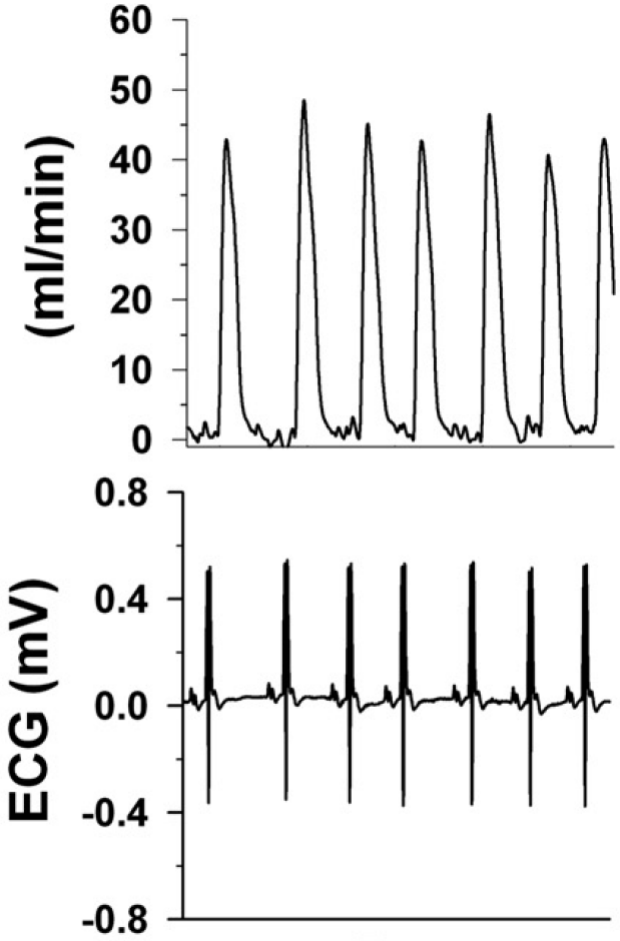

Figure 2.1: Flow waveform in ascending aorta reported in Lujan t al. [2]

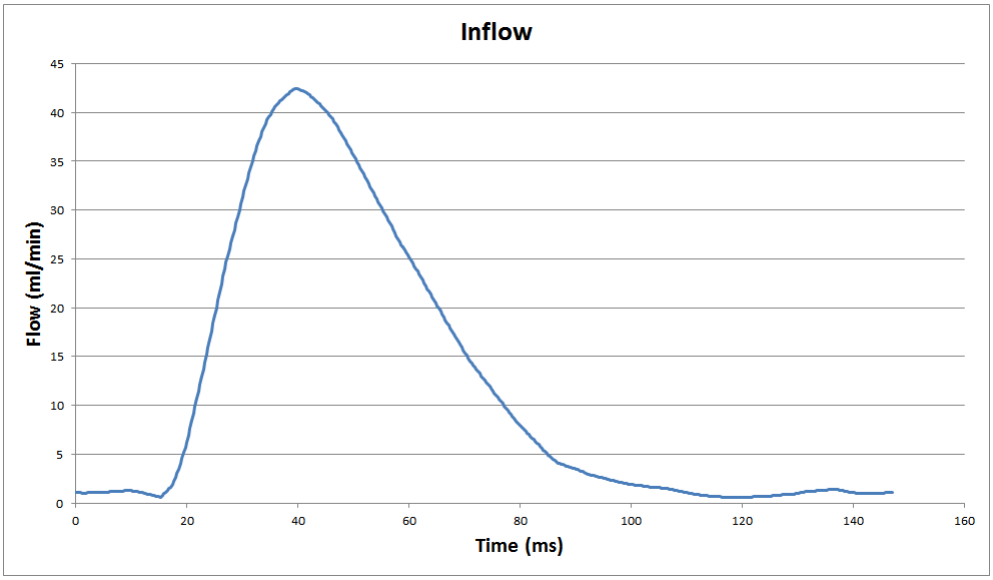

Figure 2.2: Average inflow signal obtaine from the Lujan data.

Lastly Greve et al. [4] measured blood flow in the infra-renal abdominal aorta using phase-contrast magnetic resonance imaging at 4.7 tesla in five male C57BL/6 mice, from 8 to 12 weeks old. During imaging, animals were anesthetized with isoflurane and the body temperature was maintained at 37°C using warm air. Infra-renal abdominal aortic flow was reported (see Figure 2.4).

2.1.2 Pressure data

There are two general methods to measure blood pressure in mice: non-invasive and invasive. The *tail-cuff* technique is the most used as non-invasive methodology and it has the following advantages:

- It allows repeated measurements without introducing alterations in the physiology of the animal;
- It correlates well with mean aortic pressure measured by others methods such fluid-filled catheters;
- It permits blood pressure measurements over long periods of time;

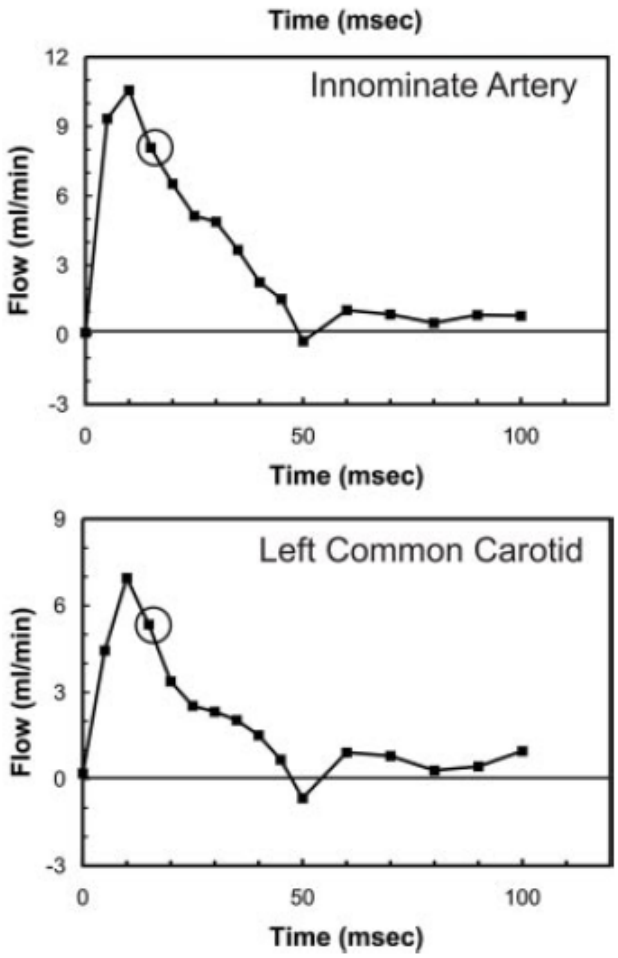

Figure 2.3: Flow data in innominate artery and left common carotid calculated from high-resolution magnetic resonance reported in Feintuch et al. Feintuch et al. [3]

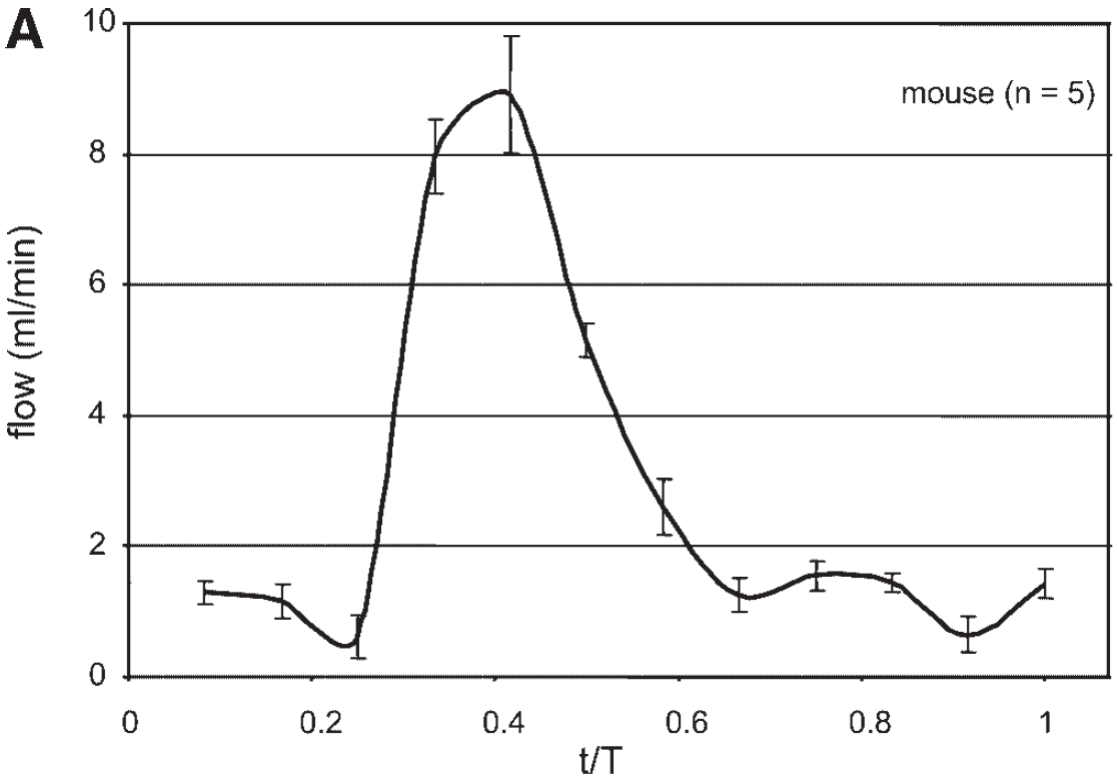

Figure 2.4: Flow data in the infra-renal abdominal aorta, Greve et al. [4]

- It makes it possible to test a large number of subjects quickly;
- It is relatively inexpensive.

The disadvantages that can restrict its use are:

- It necessitates constraint and warming of the mouse: these procedures produce stress and therefore alteration of the blood pressure;
- It shows variable results due to movement artifacts. A good matching between tail-cuff and arterial pressure is only obtained when the subject is at rest;
- It compares better with mean arterial pressure than with systolic pressure measured with invasive methods;
- The mouse need anaesthesia and this can lower the pressure readings.

Blood Pressure measurements using a tail-cuff system have been collected in a number of different inbred strains of mice and made available at the MPD web site: *http://phenome.jax.org*.
Tsukahara et al. [27] measured diastolic and systolic pressure in 15 inbred mouse strains using tail cuff. The mice were 10 weeks old. In order to collect reliable data, the mice were conditioned to blood pressure measurement and an average of 100 pressure readings in each mouse (20 measurements in 5 consecutive days) were performed. The pulse wave was recorded with a sensor (BP-98A) attached to the tail cuff. For C57BL/6J strain mice a diastolic pressure of 73.2 mmHg and a systolic pressure of 114.6 mmHg were reported.

Invasive methods allow direct measurements of arterial pressure using indwelling fluid-filled catheters, radiotelemetry systems or transducer-tipped catheters. The *implantable catheter* is set into an artery and it is associated to a pressure transducer. Some of the advantages of this technique include:

- Consistent and reproducible measurements;
- Calibration is both simple and accurate;

- Measurements over long period of time can be acquired with low stress.

Disadvantages of indwelling catheters are:

- Surgery and the use of anesthesia may cause changes in blood pressure and heart rate;
- Possible catheter occlusion;
- Potential surgical contamination;
- Limited dynamic feedback: this can affect the recording of systolic and diastolic pressures;
- Specialized surgical skills are needed.

Reddy et al. [5] evaluated the pressure in the left iliac artery using a fluid filled catheter. Five wild type mice, with an averaged body weight of 24 ± 2g were tested. The animals were anesthetized with continuous flow of isoflurane and oxygen. The values reported in Table 2.1 for systolic, diastolic and mean pressure were obtained for the iliac artery.

Systolic pressure	99 ± 15
Diastolic pressure	65 ± 11
Mean pressure	80 ± 12

Table 2.1: Iliac artery pressure measurements, Reddy et al. [5].

In a different study, Redyy et al. [6] determined input aortic impedance in adult and old mice. The mice tested were B6D2F1 type, 8 mice were 8 months old (adult) and 9 mice were 29 months old (old). The blood pressure in the ascending aorta was measured by a pressure catheter of 0.36 mm diameter, PressureWire3, RADI Medical System, Uppsala, Sweden. The catheter was positioned as close as possible to the aortic root. During the surgery the mice were anesthetized with a continuous flow of isoflurane and oxygen. Table 2.2 summerizes the experimental results.

	Adult mice	Old mice
Body weight, g	35.6 ± 0.2	34.6 ± 0.7
Heart rate, beat/min	406 ± 26	386 ± 32
Mean aortic pressure, mmHg	73 ± 7.7	92 ± 4.0
Systolic pressure, mmHg	88 ± 8.8	116 ± 4.5
Diastolic pressure, mmHg	59 ± 7.0	73 ± 3.9
Pulse pressure, mmHg	29 ± 4.9	42 ± 2.2

Table 2.2: Pressures in the aortic root measured through implantable catheter Reddy et al. [6].

Radiotelemetry systems for recording blood pressure consist of a blood pressure sensor and a transmitter. It is possible to acquire long-term measurements of unrestraint mice. This system is becoming the gold standard for blood pressure recordings in conscious mice. The advantages compared to other techniques are:

- It is possible to obtain pressure measurements in awake mice without restraints;
- Continuous recordings are possible;
- High-fidelity data;
- Long-term catheter patency;

On the other hand, it requires significant microsurgical technique skills.

Van Vliet et al. [7] used blood pressure telemeter to characterize 24h pressure in mouse lacking the gene for endothelial nitric oxide synthase and the corresponding control strain, C57BL/6J. Measurements were analyzed for the entire 24h period, and the two 12-hours periods of light and darkness. The control mice had an average weight of $27.3 \pm 0.4g$. At 9-12 weeks the animals were put in individual cages and 2 weeks later the telemeter was implanted and turned on on the 10th day. The tip of the telemeter was inserted into the aortic arch via the left carotid artery; the telemeter body was allocated subcutaneously on the right flank. During the procedure, the mice were under ketamine and xylazine anaesthesia. Table 2.3 shows the summary of the measurements.

	24h	Light period	Dark period
Mean aortic pressure, mmHg	104 ± 2	97 ± 1	110 ± 3
Systolic pressure, mmHg	119 ± 2	112 ± 2	125 ± 3
Diastolic pressure, mmHg	87 ± 2	81 ± 2	94 ± 2
Pulse pressure, mmHg	31.6 ± 1.5	31.5 ± 1.5	31.7 ± 1.5
Heart rate, beat/min	596 ± 6	556 ± 7	625 ± 9

Table 2.3: Blood pressure in the aortic arch measured through radio telemetry systems, Van Vliet et al. [7]

McGuire et al. [8] used radiotelemetry system to measure pressure in conscious unrestrained mice. As control mice they used 33 male C57BL/6J, from 10-20 weeks of age and 25-30g of weight. The room lighting was set to 12 h light and 12 h darkness cycles. The telemeter (TA11PA-C10, Datasciences Inc.) was implanted via the right carotid artery. During the surgery the animals were anesthetized with isoflurane and 13-18 days were allowed for the mice to recover. The pressure data were then recorded continuously for 3-9 days at baseline. Table 2.4 summarizes the findings of the experiments.

	12h light	12h dark
Systolic pressure, mmHg	118 ± 1	131 ± 1
Diastolic pressure, mmHg	89 ± 1	101 ± 1
Pulse pressure, mmHg	29 ± 1	31 ± 1
Heart rate, beat/min	587 ± 4	607 ± 6

Table 2.4: Blood pressure in the aortic arch measured through radio telemetry systems, McGuire et al. [8]

Lastly *transducer-tipped catheters* procure high-fidelity pressure recordings. Since measurements are taken directly at the source and are usually not affected by movement artifacts. The most used catheter is the 1.4-Fr Millar Mikro-Tip pressure transducer. This device is able to capture signals at high frequencies as the pressure changes during systole in mice. Due to the catheter stiffness, it is necessary to anesthetize or sedate the mice during the procedure. The calibration of the instrument tends to drift with time,

therefore the use of such catheters is limited to short-time recording.

Lorenz and Kranias [28] used a Millar Mikro-Tip transducer to measure pressure in the ascending aorta. Seven wild type C57B1/6 mice with an average body weight of 31g were tested. The catheter was positioned in the ascending aorta at the level of the right carotid artery. The mice were anesthetized with ketamine and thiobutabarbital during the surgical procedure. After the surgery the animal were allowed to stabilize for 30-45min. A mean average pressure of 72 mmHg and a systolic pressure of 97 mmHg are reported as baseline values for the wild type mice.

After careful consideration of the advantages and disadvantages of the different pressure recording techniques, the data reported by Van Vliet et al. [7] was chosen as gold standard in this work.

2.1.3 Geometrical data

Currently the most used technique to study the arterial geometry in mice is the vascular corrosion casting. It consists of the injection of a hardening resin in the vascular system of the animal to obtain a plastic cast that can be scanned. This technique allows to overcome the problems faced during traditional MRI of mice, since the high heart rate makes the use of contrast agents difficult. A downside of this technique is the euthanasia of the animal and therefore the inability to perform other tests on the same subject. Furthermore the reliability of the data acquired is often times questionable since the diameters can be affected by factors such as vessel tone, perfusion pressure and shrinkage of the resin used.

Vandeghinste et al. [9] investigated the differences between in vivo micro-computed tomography (CT) and the micro-CT scanning of a vascular corrosion cast. They used a new contrast agent specially developed for cardiovascular imaging in mice: Fenestra VC-131. Nine wild-type mice were tested, with body weights ranging from 14 to 35g and ages raging from 5 to 27 weeks old. The mice were first anesthetized, then scanned in vivo and one week later the casting was performed on the same animals. High-quality casts were obtained and used for four animals. The authors compared the diameters

of the vessels, the bifurcation angles and the wall shear stress levels in CFD simulations.

	Cast(mm)	In vivo(mm)	Difference(%)
Ascending aorta	1.08 ± 0.09	1.43 ± 0.07	34.21
Brachiocephalic trunk	0.55 ± 0.06	0.78 ± 0.05	41.82
Aortic arch	0.93 ± 0.05	1.24 ± 0.07	33.33
Common carotid artery	0.4 ± 0.07	0.51 ± 0.01	27.50
Subclavian artery	0.45 ± 0.05	0.62 ± 0.04	37.78
Descending aorta	0.87 ± 0.09	1.13 ± 0.09	29.89

Table 2.5: Comparison of diameters obtained with casting and in vivo micro-CT, Vandeghinste et al. [9]

The results (see table 2.5) show a significant difference (30%) in vessel diameter estimated by the two methods. The cast solution was injected without control on the pressure and therefore the perfusion pressure was likely too low. The authors hypothesized that 10% to 20% of the observed difference can be related to the large volume of contrast agent injected in the subject during the in vivo scans. This extra volume could be responsible of augmented arterial pressure in vivo. Furthermore, as no cardiac gating was applied during the study it was not possible to determine diastolic dimensions. The authors hypothesize that the in vivo diameters are close to systolic values whereas the in vitro (casting) diameters are more representative of the diastolic state.

Casteleyn et al. [10] also analyzed the mice vascular anatomy through vascular corrosion casts. Thirty female mice, 2 months old in age with a mean weight of 30.6 g were tested. The purpose of that work was to describe the anatomy and geometry of the murine heart and thoracic aorta including its main branches. After sacrificing the animals, the abdominal aorta was catheterized with a 26 gauge catheter and Batson's #17 solution was gently injected free-hand in the retrograde direction. Table 2.6 contains the summary of the results. This study has once again no perfusion pressure control and diameters are even smaller than those reported by Vandeghinste et al. [9].

Hinton et al. [11] investigated the valve structure in different phases

	Diameter(mm)
Ascending aorta	0.82 ± 0.01
Aortic Arch	1.06 ± 0.02
Descending aorta	0.74 ± 0.02
Brachiocephalic trunk	0.54 ± 0.02
Left common carotid	0.35 ± 0.02
Left subclavian	0.38 ± 0.02

Table 2.6: Vessel diameter measurements obtained by Casteleyn et al. [10]

of mouse life. The mice studied were wild-type mixed-sex C57BL6 obtained from Jackson Laboratories (Bar Harbour, ME). The life phases studied were:

- New born: 10 days
- Juvenile: 1 months
- Young adult: 2 months
- Old adult: 9 months
- Aged adult: 16 months

The body weight was measured at every step since geometric dimensions can highly vary depending on age or size. Cross-sectional, two-dimensional Doppler transthoracic echocardiography was performed by experienced sonographers using a Visual Sonics Vevo 770 Imaging System (Toronto, Canada). Mice were anesthetized with 1% to 2% isoflurane. All the reported data were averaged from three repeated measurements (see Table 2.7).

	Aortic root(mm)	Ascending aorta(mm)	Body weight(g)
10 days	0.8	0.88	7.2 ± 0.9
1 month	1.05	1.18	11.2 ± 1.0
2 month	1.23	1.39	17.3 ± 1.4
9 month	1.35	1.52	33.0 ± 6.0
16 month	1.15	1.36	26.4 ± 4.0

Table 2.7: Aortic root and ascending aorta diameters, Hinton et al. [11]

Wan et al. [12] studied increases in arterial stiffness in the common carotid artery using genetically-modified mouse models lacking fibulin-5, a critical

protein for the functionality of elastin fibers. Biaxial biomechanics test and multiphoton microscopy imaging were performed on isolated carotid arteries of seven fbln5+/+ and fbln5-/- adult C57BL/6 mice, 13 weeks old and 28.93 g body weight. The carotid were collected, dissected and put on the glass cannulae of the biomechanical testing device. Pressure-diameter data were collected from 0 to 180 mmHg at constant axial extensions. The P-d test were executed at different stretches, here the measurements collected at in vivo stretch and 100mmHg pressure are reported (see table 2.8).

	In vivo dimensions(mm)
Inner diameter	0.603
Outer diameter	0.652
Wall thickness	0.024

Table 2.8: Carotid diameters obtained via biaxial tissue testing by Wan et al. [12]

Trachet et al. [13] used micro-CT scans to investigate the anatomy of the abdominal aorta and its main branches in mice. They also utilized high-frequency ultrasound imaging to acquire flow information in each branch. Ten C57BL/6 ApoE-/- mice, 12 ± 3 weeks old, were studied. An osmotic pump was implanted to continuously infuse Angiotensin II, to induce the development of an abdominal aneurysm. Measurements were taken before pump implantation and after 31 days. To perform the micro-CT, the mice were anesthetized with 1.5% isoflurane and 100 microliter/25g of Aurovist was injected intravenously. See Table 2.9 for results.

BW,g	HR,bpm	PAA	CEL	MES	RREN	LREN	DAA
24.4	444	1.24	0.43	0.65	0.54	0.43	0.73

Table 2.9: Mean diameters reported by Trachet et al. [13]. BW: body weight, HR: heart rate, PAA: proximal abdominal aorta, CEL : celiac artery, MES: mesenteric artery, RREN: right renal artery, LREN: left renal artery, DAA: distal abdominal artery. The diameters are reported in mm.

A summary of the data used in this work is reported in the table 2.10. The age and the size of the animals tested have been taken into account in the choice, since they strongly affect the geometrical dimension.

LOC	Original casting diameter	Literature diameter	Description of methodology
AAo	0.9153	1.43	Vandeghinste (2011) [9]; in vivo micro-CT. The diameter is calculated as mean of a large area.
AA	0.8347	1.24	Vandeghinste (2011) [9]; in vivo CT. The diameter is calculated as mean of a large area.
DA	0.6842	1.13	Vandeghinste (2011) [9]; in vivo micro-CT. The diameter is calculated as mean of a large area.
IN	0.4573	0.78	Vandeghinste (2011) [9]; in vivo micro-CT. The diameter is calculated as mean of a large area.
LCC	0.2701	0.51	Vandeghinste (2011) [9]; in vivo micro-CT. The diameter is calculated as mean of a large area.
LSUB	0.2989	0.62	Vandeghinste (2011) [9]; in vivo micro-CT. The diameter is calculated as mean of a large area.
CEL	0.2756	0.43	Trachet (2011)[13]; micro-CT scans.
MES	0.2985	0.65	Trachet (2011)[13]; micro-CT scans.
RREN	0.30	0.54	Trachet (2011)[13]; micro-CT scans.
LREN	0.2309	0.43	Trachet (2011)[13]; micro-CT scans.

Table 2.10: The location, the diameter of the model and the diameter of the best reference are reported. AAo: ascending aorta, AA: aortic arch, DA: descending aorta, IN: innominate artery, LCC: left common carotid, LSUB: left subclavian, CEL: celiac artery, MES: mesenteric artery, RREN: right renal artery, LREN: left renal artery. Measurements reported in mm.

2.2 Building the 3D geometric mouse model

2.2.1 Original geometry

A 3-D model of the mouse arterial geometry was built using the custom software Simvascular; using micro-CT imaging of a vascular casting of a,27.14 weeks old, 42.64 g, mouse. The vascular corrosion casting and the corresponding geometric model were obtained at the Department of Biomedical Engineering of Yale University, New Haven, CT, USA.

Briefly, the mouse was anesthetized using sodium pentobarbital, the left ventricle was cannulated at its apex using with a 25-G needle and the major distal vessels (subclavians, carotids, renals and iliacs) were ligated. The aorta was then flushed with heparinized saline (110 U/Kg). This precasting treatment is necessary in order to completely remove the blood from the target vessel. The goal is then to fill the entire vascular bed and to obtain endothelial cell imprints on the surface of the cast [29]. The aortic tree was perfused at a fixed pressure of 100mmHg for 2 hours with 4% paraformaldehyde follwed by injection of Batson's no. 17 Plastic replica Kit (Polysciences, WA) for 2.5 hours using the manufacturers specifications. It is critical to adjust the injection pressure in order to fill the vascular bed completely. The plastic cast was then gently excised and placed in a KOH solution to remove adherent tissue. The geometry of the aortic tree was then imaged using micro-CT.

SimVascular allows users to generate geometric models from imaging data. During the segmentation procedure, the arterial lumen boundary is defined using a combination of manual demarcation, image thresholding, and level-set segmentation [30]. To perform the segmentation a set of vessel centerline paths are created and then 2-D segmentations are built along each path (see Figure 2.5). A 3-D geometric solid model is created by lofting the 2-D segmentations with Non-Uniform Rational B-Splines (NURBS).

The mouse vasculature model includes the ascending, descending, and abdominal aorta and significant segments of the subclavians, the carotids, the renal arteries, mesenteric, celiac, and tail; see Figure 2.6.

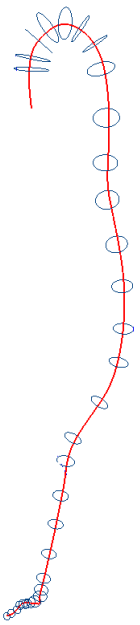

Figure 2.5: Path along the aorta and 2-D segmentations of the vessel lumen.

2.2.2 Up-scaled model

In the casting process, the injection pressure was insufficient and consequently the vessel diameters were too small relative to the reference values given in Table 2.10.

Understimation of the vessel caliber has a very negative impact on the computed hemodynamics. When a physiological flow waveform is pushed through the under-represented geometry, the resulting pulse pressure is much higher than what is observed physiologically. This is of course due to the artificially high resistance of the narrower than normal vessels. Furthermore, these big resistances makes it difficult to choose boundary condition parameters required to obtain the desired flow splits. We have therefore modified the vessel diameters to match the literature data presented earlier. For each segmentation, a centroid and mean radius were calculated. The mean radius for each vessel was then scaled up to match the dimensions reported in Table 2.10. A different scaling factor was used for each segmentation. The aorta was upscaled using three reference diameters: the ascending aorta, the aortic

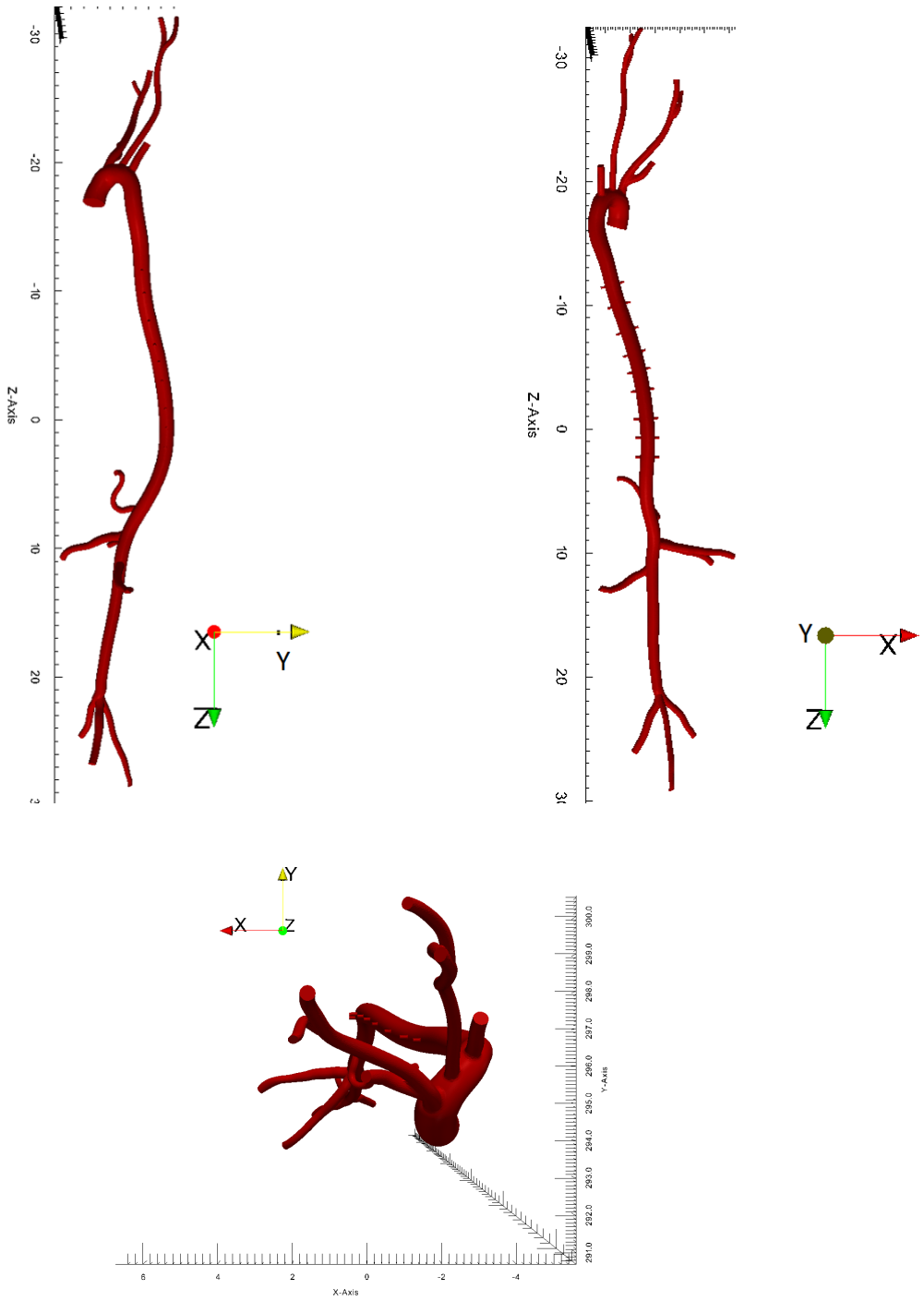

Figure 2.6: Lateral, anterior, and axial views of the 3D Model built from the micro-CT imaging of the corrosion cast

arch and the descending aorta such that each reference radius is the mean of the radii in a given section of the vessel. For those vessels for which a reference diameter was not available, the scale factor of the closest segmentation was used to scale all segmentations in that vessel (see Figure 2.7).

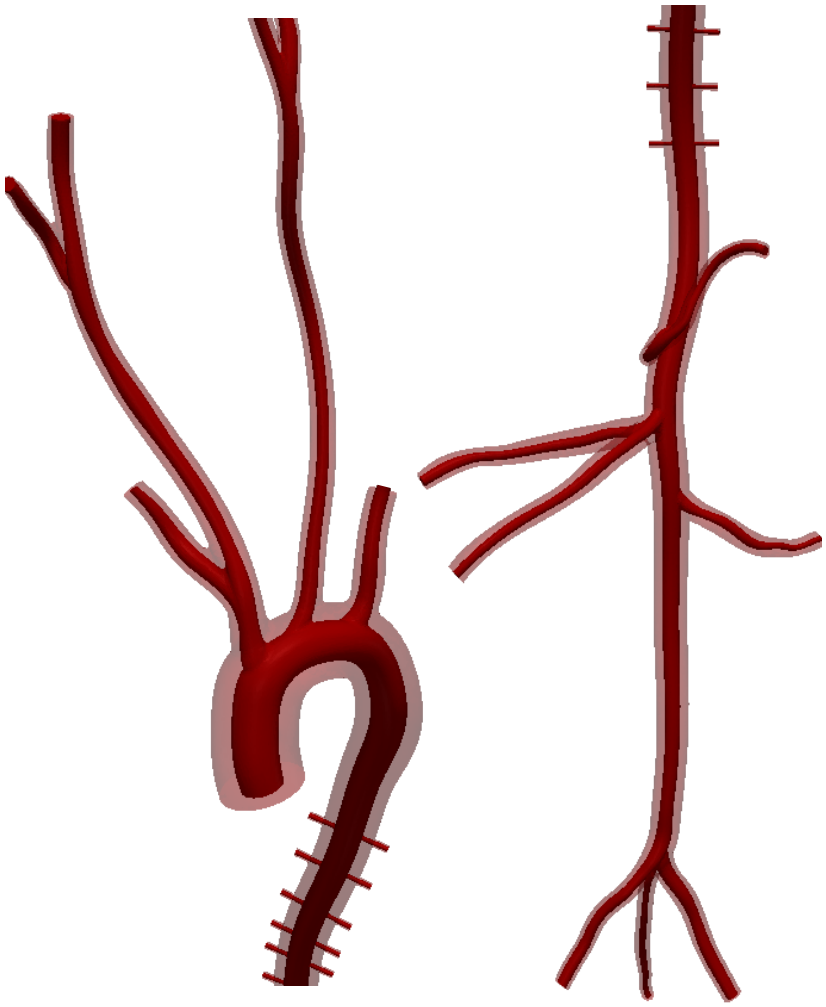

Figure 2.7: View of the original geometry (inner) and the upscaled geometry (external overlay).

2.2.3 Intercostal arteries

The image data did not allow for visualization of the intercostal arteries, which take up a blood flow up to 17.3% of the mouse cardiac output [**?**]. In the interest of making the pressure gradient across the thoracic aorta and the flow distributions more realistic, intercostal arteries were added to the model using reference diameters and branch distances [14]. For each of the nine pairs of intercostal arteries, the branch distance was defined as the relative length along the aorta path spline (see Table 2.11). The branch origin was calculated using the mean of the centers of the two nearest aorta segmentations, weighted by the relative distance to each segment. The intercostal paths were defined as straight lines parallel to the branching angle of the corresponding renal artery, perpendicular to the aorta path, and with a length of twice the aorta diameter at that point.

Fractional longitudinal position	Location down the aorta
0	Aortic semilunar valve
0.20 ± 0.013	First pair of intercostal arteries
0.24 ± 0.014	Second pair of intercostal arteries
0.29 ± 0.0066	Third pair of intercostal arteries
0.34 ± 0.0087	Fourth pair of intercostal arteries
0.38 ± 0.0080	Fifth pair of intercostal arteries
0.42 ± 0.0064	Sixth pair of intercostal arteries
0.47 ± 0.0087	Seventh pair of intercostal arteries
0.51 ± 0.0096	Eighth pair of intercostal arteries
0.55 ± 0.012	Ninth pair of intercostal arteries
1	Common iliac artery

Table 2.11: Fractional longitudinal position of the intercostals on branch vessel along the aorta, Guo et al. [14]

2.3 Computational fluid dynamics method

2.3.1 Mesh and mesh adaptivity

Good quality computational grids are needed to ensure a proper numerical simulation. An initial mesh was generated using the meshing libraries in Simvascular. A global value for the element size of 0.08 mm was used together with a refinement on the intercostal arteries. Boundary layer meshing was also used in order to ensure good density of elements close to the vessel wall, where all the action happens. With these parameters a 2 million element mesh was obtained.

This mesh was used to run a rigid simulation for 2 cardiac cycles using 1470 time steps per cycle ($T_{cycle} = 0.147s$). The results of this first simulation were used to adapt the mesh taking into account the distribution of velocity gradients in the arterial network. The adaptation mesh algorithm reduces the number of elements in regions of low velocity gradients and increases the number of elements in areas of large velocity gradients. The objective of this "a-posteriori" error estimation-based mesh adaptivity technique is to obtain a uniform distribution of error in all spatial directions. This mesh adaptation operation reduced the number of elements in the initial mesh to less than 1 million (see Figure 2.8). This reduction of number of elements allows to decrease prominently the time to complete the same simulation to one third of the time required to solve the same problem on the initial mesh.

2.3.2 Multiscale modelling approach

The 3-D equations representing the flow of an incompressible Newtonian fluid are the so-called Navier-Stokes equations of motion and mass continuity, together with adequate initial and boundary conditions. The weak form is reported:

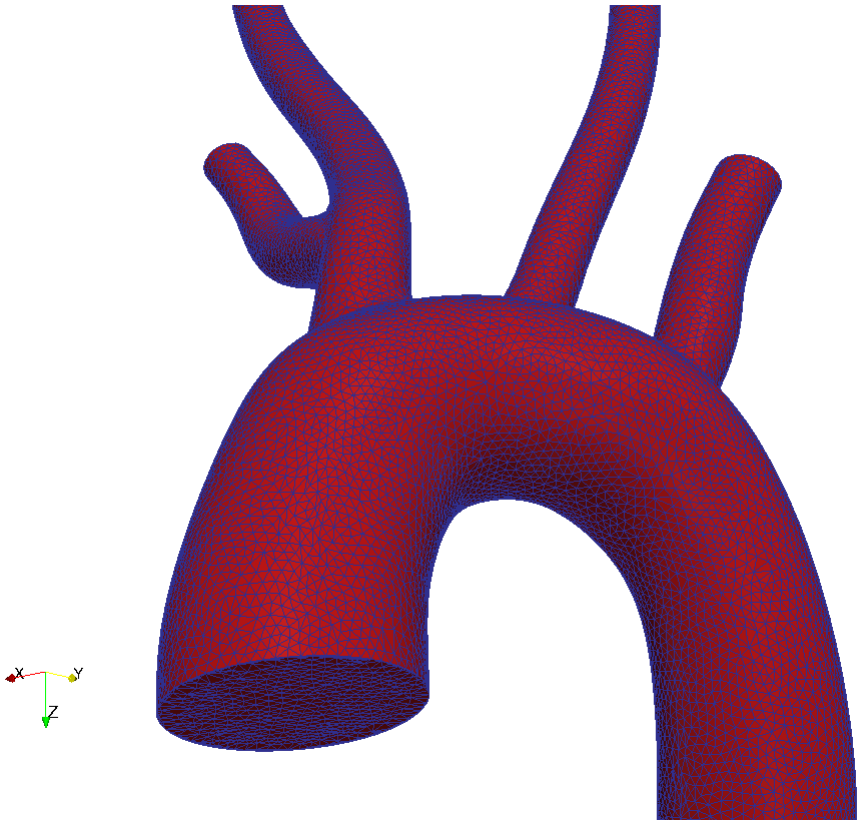

Figure 2.8: Partial view of the mesh after mesh adaptivity.

$$\int_\Omega \{\mathbf{w}\cdot(\rho\mathbf{v}_{,t}+\rho\mathbf{v}\cdot\nabla\mathbf{v}-\mathbf{f})+\nabla\mathbf{w}:(-p\underset{\sim}{I}+\underset{\sim}{\tau})\}d\mathbf{x} \tag{2.1}$$
$$-\int_\Omega \nabla q\cdot\mathbf{v}d\mathbf{x}-\int_{\Gamma_{out}}\mathbf{w}\cdot(-p\underset{\sim}{I}+\underset{\sim}{\tau})\cdot\mathbf{n}ds+\int_\Gamma q\mathbf{v}\cdot\mathbf{n}ds$$

where $\mathbf{v}$ and p are the fluid velocity and pressure, $\mathbf{f}$ is a body force, $\mathbf{w}$ and q are weighting functions, and ρ is the blood density. Ω is the fluid domain, whose boundary Γ is split into a Dirichlet partition Γ_{in}, Neumann partitions Γ_{out} and Γ_t such that $\Gamma=\partial\Omega=\Gamma_{in}\cup\Gamma_{out}\cup\Gamma_t$ and $\Gamma_{in}\cap\Gamma_{out}\cap\Gamma_t=\emptyset$.

A coupled multi-domain method is used [31] in order to represent the entire arterial vasculature from the central aorta to the capillaries. This method employs a decomposition of the spatial domain Ω into an upstream "numerical" domain $\hat{\Omega}$, and a downstream "analytical" domain Ω' such that $\hat{\Omega}\cap\Omega'=\emptyset$ and $\overline{\hat{\Omega}\cup\Omega'}=\Omega$ (see Figure 2.9). These two domains are separated by the interface Γ_{out}. A similar decomposition is applied to the variables fluid velocity $\mathbf{v}=(v_x,v_y,v_z)$ and pressure p. The solution vector $\mathbf{V}=\{\mathbf{v},p\}^T$ is separated into a component defined within the numerical domain $\hat{\Omega}$ and a component defined within the analytical domain Ω':

$\mathbf{V}=\hat{\mathbf{V}}+\mathbf{V'}$ with $\hat{\mathbf{V}}|_{\Omega'}=0$ and $\mathbf{V}'|_{\hat{\Omega}}=0$

This decomposition satisfies the condition $\hat{\mathbf{V}}=\mathbf{V}'$ at the interface Γ_{out}, and is also applied to the weighting functions. This decomposition will allow different degrees of solution resolution in the two domains. $\hat{\Omega}$ represents the 3-D domain in which the Navier-Stokes equations for an incompressible Newtonian fluid are solved. Ω' corresponds to the distal vascular network and microcirculation where the flow physics are described using a lumped-parameter formulation.

The coupled-multidomain method produces a variational form for the numerical domain similar to the one given by the Eq. 2.1, where the integral term defined on Γ_{out} is written in terms of operators $M=\{M_m,M_C\}^T|_{\Gamma_{out}}$ and $H=\{H_m,H_C\}^T|_{\Gamma_{out}}$

$$\int_{\hat{\Omega}} \hat{\mathbf{w}} \cdot (\rho \hat{\mathbf{v}}_{,t} + \rho \hat{\mathbf{v}} \cdot \nabla \hat{\mathbf{v}} - \mathbf{f}) + \nabla \hat{\mathbf{w}} : (-\hat{p} \underset{\sim}{I} + \hat{\underset{\sim}{\tau}}) d\mathbf{x} \tag{2.2}$$
$$- \int_{\Gamma_{out}} \hat{\mathbf{w}} \cdot (\underset{\sim}{M}_m(\hat{\mathbf{v}}, \hat{p}) + \underset{\sim}{H}_m) \cdot \hat{\mathbf{n}} ds - \int_{\hat{\Omega}} \nabla \hat{q} \cdot \hat{\mathbf{v}} d\mathbf{x} + \int_{\hat{\Gamma}} \hat{q} \hat{\mathbf{v}} \cdot \hat{\mathbf{n}} ds$$
$$+ \int_{\Gamma_{out}} \hat{q} (\mathbf{M}_C(\hat{\mathbf{v}}, \hat{p}) + \mathbf{H}_C) \cdot \hat{\mathbf{n}} ds = 0$$

where subscripts m and c denote the fluid momentum and mass balance components of the operators, respectively. These operators are defined in the domain Ω' based on the model chosen to represent blood flow and pressure in the distal analytical domain.

In this work a three-component Windkessel model has been adopted: this requires the definition of a proximal resistance R_p, compliance C and distal resistance R_d. These three parameters are used to define the operators M and H [26].

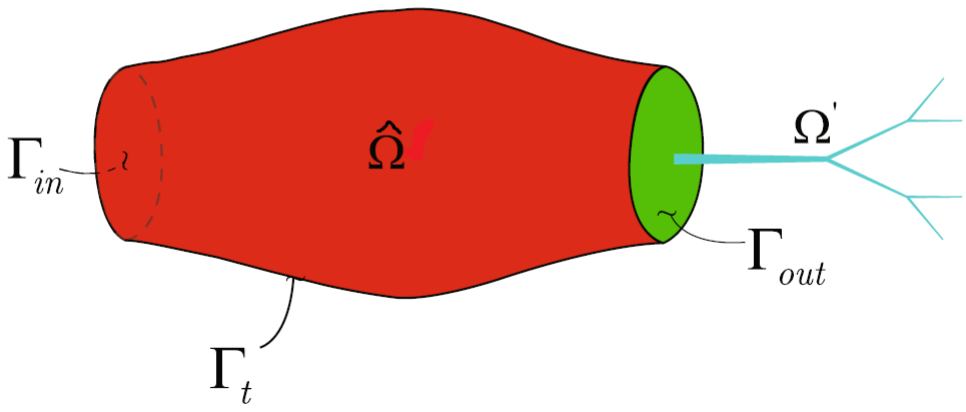

Figure 2.9: The overall fluid domain Ω is separated into an upstream numerical domain $\hat{\Omega}$ and a downstream analytical domain Ω', demarcated by the interface Γ_{out}.

2.3.3 Fluid-structure interaction

The majority of computational fluid dynamics simulation in mice [3] [13] [24] have assumed rigid arterial walls, which disallows accurate calculations of blood pressure despite possibly achieving good estimates of velocity field. We are interested in pulse pressure estimation and pulse wave velocity which are fundamental to study the relationship between arterial stiffening and hypertension. In order to capture pulse pressure propagation is mandatory to use fluid structure interaction (FSI). Effectively, wave propagation phenomena in the cardiovascular system can only be described considering wall deformability since blood is described as an incompressible fluid. In this work the FSI "Coupled Momentum" method developed by Figueroa and Taylor at Stanford, was used. The method starts from the conventional stabilized finite element formulation for the Navier-Stokes equations in a rigid domain (see Eq. 2.1) (Figueroa et al. [16]). The method then incorporates the elastodynamic equations representing the deformation of the wall over a cardiac cycle as a boundary condition for the fluid domain. The degrees-of-freedom of the fluid and the solid domains are strongly coupled. The effect of the vessel wall boundary is added in a monolithic way to the fluid equations. It employs a linearized stiffness and membrane model for the vessel wall resulting in a robust scheme with minimal computational cost beyond that required for rigid wall problems. The zero-velocity Dirichlet condition prescribed on the lateral boundary in rigid wall formulations is replaced by a Neumann condition which is the traction originating from interactions with the vessel wall. The weak form of the governing equations for the fluid domain can be written as:

$$\begin{aligned}
&\int_{\Omega} \{\mathbf{w} \cdot (\rho \mathbf{v}_{,t} + \rho \mathbf{v} \cdot \nabla \mathbf{v} - \mathbf{f}) + \nabla \mathbf{w} : (-p\underset{\sim}{I} + \underset{\sim}{\tau}) - \nabla q \cdot \mathbf{v}\} d\mathbf{x} \qquad (2.3)\\
&+ \int_{\Gamma_{out}} \{-\mathbf{w} \cdot \mathbf{t} + q v_n\} ds + \int_{\Gamma_{in}} q v_n ds\\
&+ h \int_{\Gamma_t} \{-\mathbf{w} \cdot \rho^s \mathbf{v}_{,t} + \nabla \mathbf{w} : \underset{\sim}{\varrho}(\mathbf{u})\} ds - h \int_{\partial \Gamma_{out}} \mathbf{w} \cdot \mathbf{t}^s dl + \int_{\Gamma_t} q v_n ds.
\end{aligned}$$

Where h is the arterial thickness, ρ^s the density of the arterial wall, $\mathbf{t}$ is

a traction boundary condition four the fluid outflow face and $\mathbf{t}^s$ is a traction boundary condition for the wall on the outlet. Using a deformable wall model, an accurate description of the constitutive behavior of the tissue is necessary. The arterial wall is modeled as a thin, incompressible, homogenous, isotropic, linear elastic membrane characterized by an elastic modulus E, a Poisson ratio $\nu = 0.5$ and a thickness h. It is necessary to characterize structural stiffness of the vessel, hence the young modulus E and the wall thickness h. The local thickness h was defined as 10% of the local radius r [1]. Biaxial stiffness values in four different locations were experimentally obtained in the Department of Biomedical Engineering of Yale University. Linearized stiffness values at in vivo axial stretch and pressure of 100mmHg were measured for ascending, descending and abdominal aorta, as well as right common carotid artery. The stiffness matrixes are reported in Figure 2.10. In this work, we used the calculated circumferential stiffness as a surrogate of isotropic stiffness, since it is the component that mostly affects radial deformation. In future work, we will consider the full biaxial stiffness. The three aortic measurements were interpolated to define stiffness values for each element of the mesh along the aorta. The value of the left common carotid was used for upper and lower branches (see Figure 2.11). In order to study the effects of increased stiffness on the hemodynamics, the structural stiffness of the wall was also increased to represent age-related changes. Two additional simulations were run by scaling the young modulus E by a factor of 2 and 3, respectively.

2.3.4 Tissue support

Another important aspect to take into account in the FSI simulation is the support exerted by the perivascular tissue and other organs on the arterial wall. This tissue support helps to prevent non physiological oscillations in the movement of arterial wall. A simple traction is applied on the outer boundary of the vessel wall to represent the mechanical behavior of the perivascular tissue [32]. This traction boundary condition consists of a viscoelastic term with two parameters (a stiffness and a viscous parameter) that can be ad-

Ascending aorta, λ=1.71

$$K = \begin{vmatrix} 1.987 & 0.767 & 0 & 0 & 0 \\ 0.767 & 1.758 & 0 & 0 & 0 \\ 0 & 0 & 1.066 & 0 & 0 \\ 0 & 0 & 0 & 0.312 & 0 \\ 0 & 0 & 0 & 0 & 0{,}287 \end{vmatrix}$$

Descending aorta, λ=1.50

$$K = \begin{vmatrix} 3.145 & 0.610 & 0 & 0 & 0 \\ 0.610 & 1.232 & 0 & 0 & 0 \\ 0 & 0 & 0.804 & 0 & 0 \\ 0 & 0 & 0 & 0.195 & 0 \\ 0 & 0 & 0 & 0 & 0.191 \end{vmatrix}$$

Infra-renal abdominal aorta, λ=1.66

$$K = \begin{vmatrix} 3.175 & 0.671 & 0 & 0 & 0 \\ 0.671 & 1.232 & 0 & 0 & 0 \\ 0 & 0 & 0.868 & 0 & 0 \\ 0 & 0 & 0 & 0.226 & 0 \\ 0 & 0 & 0 & 0 & 0.167 \end{vmatrix}$$

Right common carotid artery, λ=1.74

$$K = \begin{vmatrix} 2.727 & 0.917 & 0 & 0 & 0 \\ 0.917 & 1.279 & 0 & 0 & 0 \\ 0 & 0 & 1.090 & 0 & 0 \\ 0 & 0 & 0 & 0.201 & 0 \\ 0 & 0 & 0 & 0 & 0.147 \end{vmatrix}$$

Figure 2.10: Biaxial stiffness values in four different location measured at in vivo axial stretch λ and pressure=100mmHg.

justed to mimic the response of various physiological tissues.

2.4 Boundary condition specification

The three-element Windkessel model coupled at each outlet of the 3-D domain is an electrical circuit analogue of the circulation (0-D) composed of a resistance R_1 connected in series with a parallel of a resistance R_2 and a compliance C (see Figure 1.3). This model represents the small arteries and arterioles, down to the capillary level. The pressure and the flow at each Windkessel are related by the following ODE:

$$Q(1 + \frac{R_1}{R_2}) + CR_1\frac{\partial Q}{\partial t} = \frac{P - P_{out}}{R_2} + C\frac{\partial P}{\partial t} \tag{2.4}$$

where P_{out} is the pressure at the micro circulation (assumed to be zero here). This Windkessel model prescribes a weak pressure on the outlet of the 3-D domain for a given flow. For details on the specific implementation see Vignon-Clementel et al. [26].

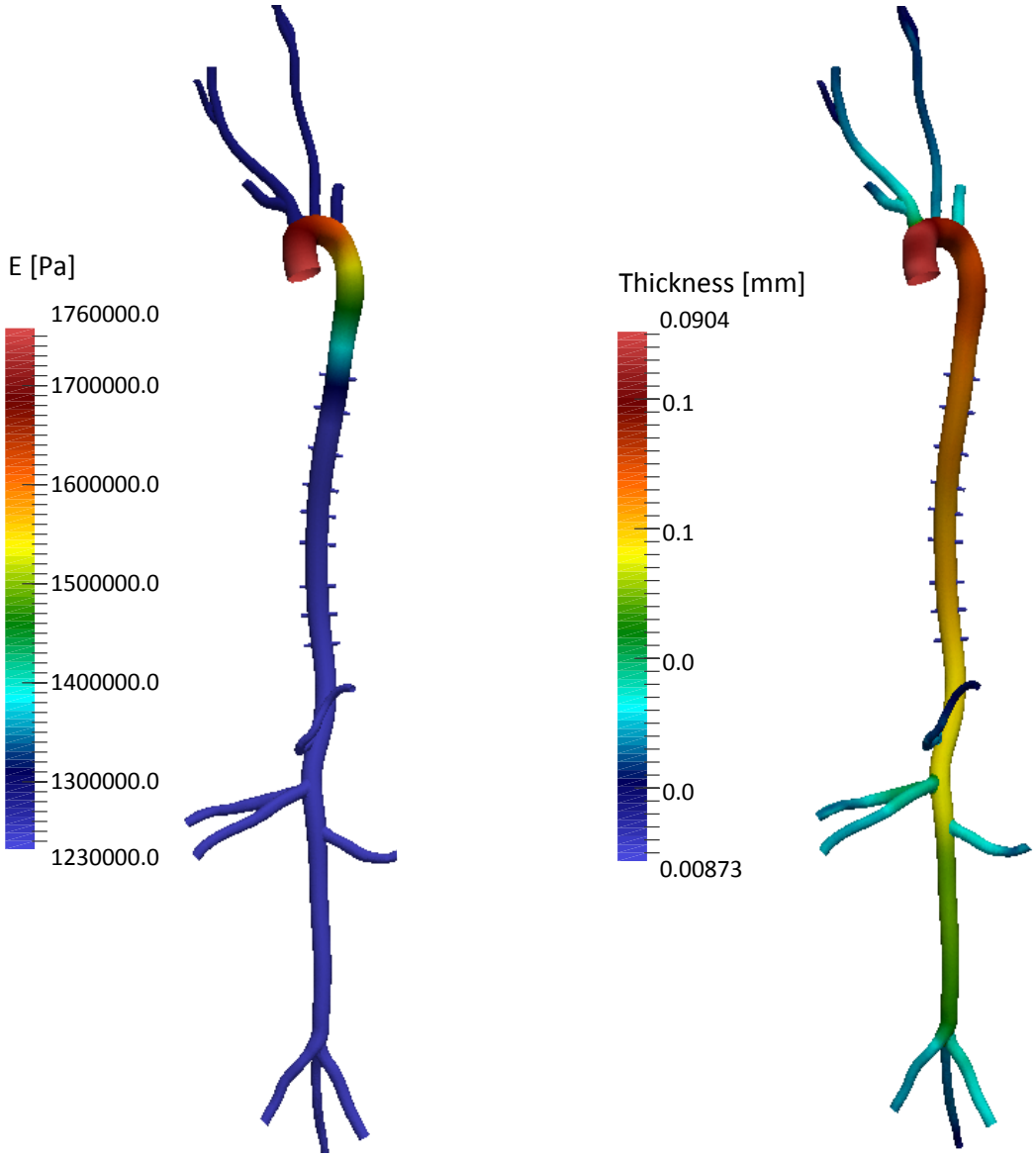

Figure 2.11: Tissue properties: young modulus interpolated from the data acquired at Professor Humphrey's lab and thickness defined as 10% of the local radius.

The parameters of the Windkessel model have been computed to reach the target diastolic and systolic pressure P_d,P_s (see section 2.1.2). The initial estimation of total resistance of the system is calculated as:

$$R_T = \frac{P_m - P_{out}}{Q_{mean}} \tag{2.5}$$

where Q_{mean} is the mean inflow and P_m is the mean blood pressure, assumed uniform throughout the arterial network. R_T represents the total resistance of the model (combination of the 3-D geometry and the distal Windkessel model). We started off assuming that the resistance of the 3-D domain is much smaller than the 0-D domain. The distribution of the total resistance $R_j = R_1^j + R_2^j$ for each outlet j of the model has been derived using the relationship

$$\frac{1}{R_T} = \sum_j \frac{1}{R^j} \Rightarrow \frac{R_T}{R^j} = \frac{Q^j}{Q_{mean}} \Rightarrow R^j = R_T \frac{Q_{mean}}{Q^j} \tag{2.6}$$

For each outlet the proximal resistance R_1^j is assumed to be equal to the characteristic impedance at the outlet of the upstream domain

$$R_1^j = \frac{\rho_f c_d^j}{A_d^j} \tag{2.7}$$

where c_d^j is the wave speed and A_d^j the reference area at diastolic pressure. This choice minimizes the amount of wave reflection at the outlet. The distal resistance R_2^j for each outlet is then calculated as $R_2^j = R^j - R_1$.

The total compliance of the model C_T is calculated using the approximation $C_T = \frac{dV}{dP}$:

$$C_T = \frac{Q_{max} - Q_{min}}{P_s - P_d} \Delta t \tag{2.8}$$

where Q_{max} and Q_{min} are the maximum and minimum inlet flow rates and Δt is the difference between the time at Q_{max} and the time at Q_{min}.

The total compliance C_T is then split between C_c (total compliance of

the 3-D model) and C_p (total peripheral compliance): $C_T = C_c + C_p$.
C_c is the sum of the compliance of each vessel, which is calculated as

$$C_c^j = \frac{A_d^j L^j}{\rho_f (c_d^j)^2} \tag{2.9}$$

where L^j is the length of the vessel j.

The total peripheral compliance is then calculated as $C_p = C_T - C_c$. This compliance is distributed among the different outlets in proportion to the flow distribution.

$$\frac{Q_j}{Q_{mean}} = (\frac{R_2^j}{R_1^j})\frac{C_p^j}{C_p} \Rightarrow C_p^j = C_p \frac{Q_j}{Q_{mean}}(\frac{R_1^j + R_2^j}{R_2^j}) \tag{2.10}$$

Lastly, the wave speed c^j at each outlet is estimated using two different procedures, depending on the information available on the mechanical properties.

- If stifness E and thickness h are known:

$$c^j = \sqrt{\frac{\beta^j}{2\rho A_d^j}}(A_d^j)^{1/4}; \beta^j = \frac{4}{3}\sqrt{\pi} E^j h^j \tag{2.11}$$

- If stifness E and thickness h are not known (as in the case of rigid wall analyses):

$$c^j = \frac{a_2}{(2R_d^j)^{b_2}} \tag{2.12}$$

  The value of c_j is given in m/s. This is a non-dimensionally consistent empirical formula [33]; where $a_2 = 13.3$ and $b_2 = 0.3$.

Chapter 3

Results

In this chapter the more significant results of the four simulations run are presented.

3.0.1 Baseline model

The first simulation correspond to a baseline model. The Windkessel parameters obtained following the procedure detailed in section 2.4 are reported in Table 3.1. The vessel wall density was $\rho = 1.06 g/cm^3$, the Poisson's ratio $\nu = 0.5$, and the transverse shear factor $k = 0.833$. A representative ascending aortic flow waveform (see Fig. 2.2) with an average cardiac output of 11.92 mL/min and a cardiac cycle of 0.147 s was prescribed. The finite element mesh consisted of 986,122 linear tetrahedras and 202,976 nodes. A time step size of 0.01 ms was used and the simulation was run for eight cardiac cycles to achieve cycle-to-cycle periodicity in the results.

The peak systolic map for the wall shear stress, the volume rendering of the velocity magnitude and pressure are shown in Figure 3.1.

There is a good agreement between simulated regional flow distributions and reported values in literature as shown in Table 3.2. However, the time-resolved flow waveforms at different sites in the model exhibit different qualitative characteristics compared to data found in literature (see Fig. 3.2). This discrepancy can be reduced by further tunning of outflow boundary conditions.

	R_p	C	R_d
Celiac	67.84	338.24	1479.07
Intercostals	356.22	68.20	7334.46
Left ext. carotid	67.93	255.16	1616.13
Left int. carotid	62.90	349.94	1178.41
Left iliac	26.79	719.08	877.94
Left renal	44.99	555.17	901.12
Left subclavian	32.12	690.06	724.98
Mesenteric	35.39	673.20	743.14
Right ext. carotid	143.85	219.65	2008.58
Right int. carotid	39.78	468.33	942.03
Right iliac	39.77	560.49	1126.35
Right renal	42.15	554.69	901.91
Right subclavian	55.54	444.62	992.28
Tail	78.83	321.06	1966.32

Table 3.1: Windkessel parameters in the baseline simulation. The resistances are expressed in $\frac{Pa \cdot s}{mm^3}$ and the compliance in $10^{-6}\frac{mm^3}{Pa}$.

Location	%CO Simulation	%CO Reference
Innominate artery	17.09	17
Left common carotid	9.46	9.76
Infra-renal aorta	17.06	17.1

Table 3.2: Simulated and reference values of %CO

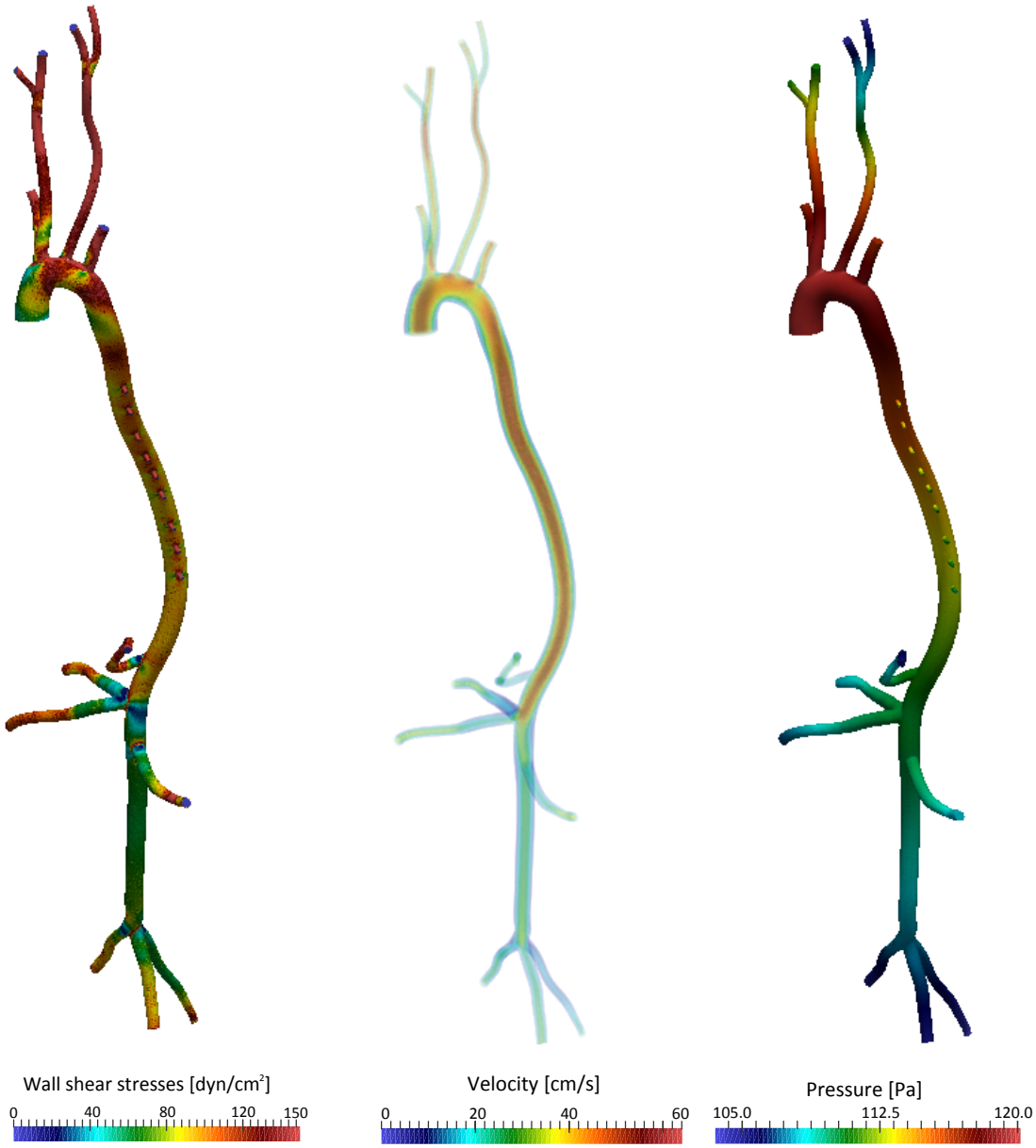

Figure 3.1: Magnitude of the wall shear stress, volume rendering of the velocity magnitude and pressure at the peak systolic.

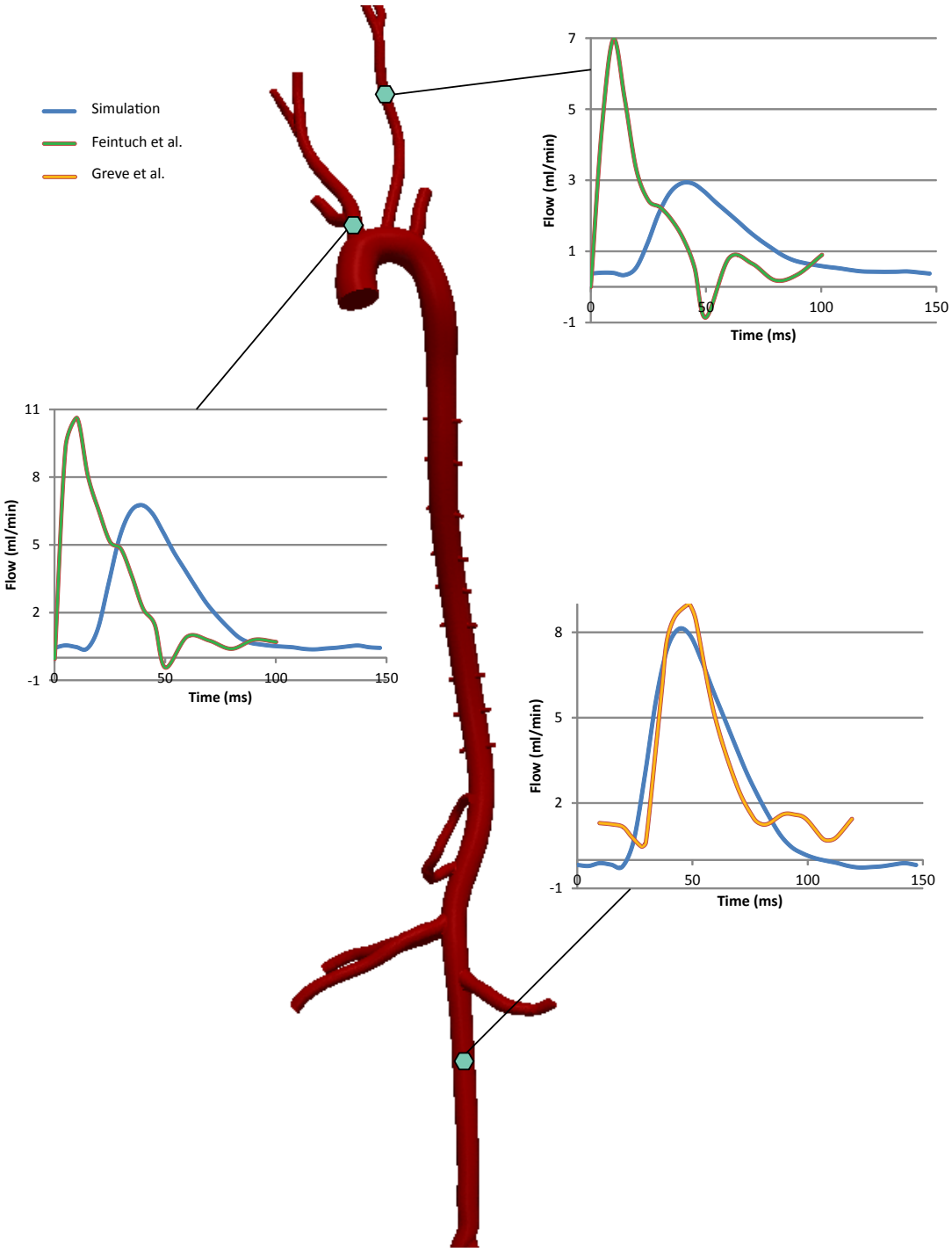

Figure 3.2: Flow waveforms compared to literature data at representative locations in the model

Figure 3.3 shows pressure waveform at seven sites along the aorta. The shape and pressure range of the waveform match data reported in literature [34]. Indeed, the pressure rises in the systolic phase and then falls in an almost exponential fashion. Pressure in the ascending aorta ranged from 93 to 120 mmHg. No increase in pulse pressure is observed down the aorta: all seven locations exhibit similar amplification and contour. We therefore reproduced reported literature data indicating lack of pressure pulse amplitude down the aorta in mice [1].

3.0.2 Modified distal compliance case

Another simulation was run to investigate whether amplification of the pulse is physiologically obtainable. We thus modified RCR values derived from the 1-D theory (see Section 2.4) reducing the compliance of the distal vessel (tail, iliacs, mesenteric, renals and celiac arteries) by a factor of 5.
Figure 3.4 shows how this change of RCR values leads to an augmentation in pulse pressure along the aorta as desired: The proximal pulse pressure is 30 mmHg, while the distal pulse pressure is 34 mmHg.

3.0.3 Increased arterial stiffness

The impact of temporal changes in wall mechanical properties, due to aging and hypertension, on pressure pulse propagation has also been investigated. It is known that in mice, as in humans, aging increases aortic wall thickness and collagen remodeling [17].Two additional simulations in which arterial stiffness was increased to represent age-related changes in mechanical properties were performed. These two additional cases were obtained by scaling the distribution of stiffness E of the baseline case by a factor of 2 and 3, respectively. In these two cases the values of RCR were identical to the baseline case, since the aging changes are observed to be largest in the aorta and in central arteries. Figure 3.5 shows pressure waveforms at seven sites in the aorta for all three cases.

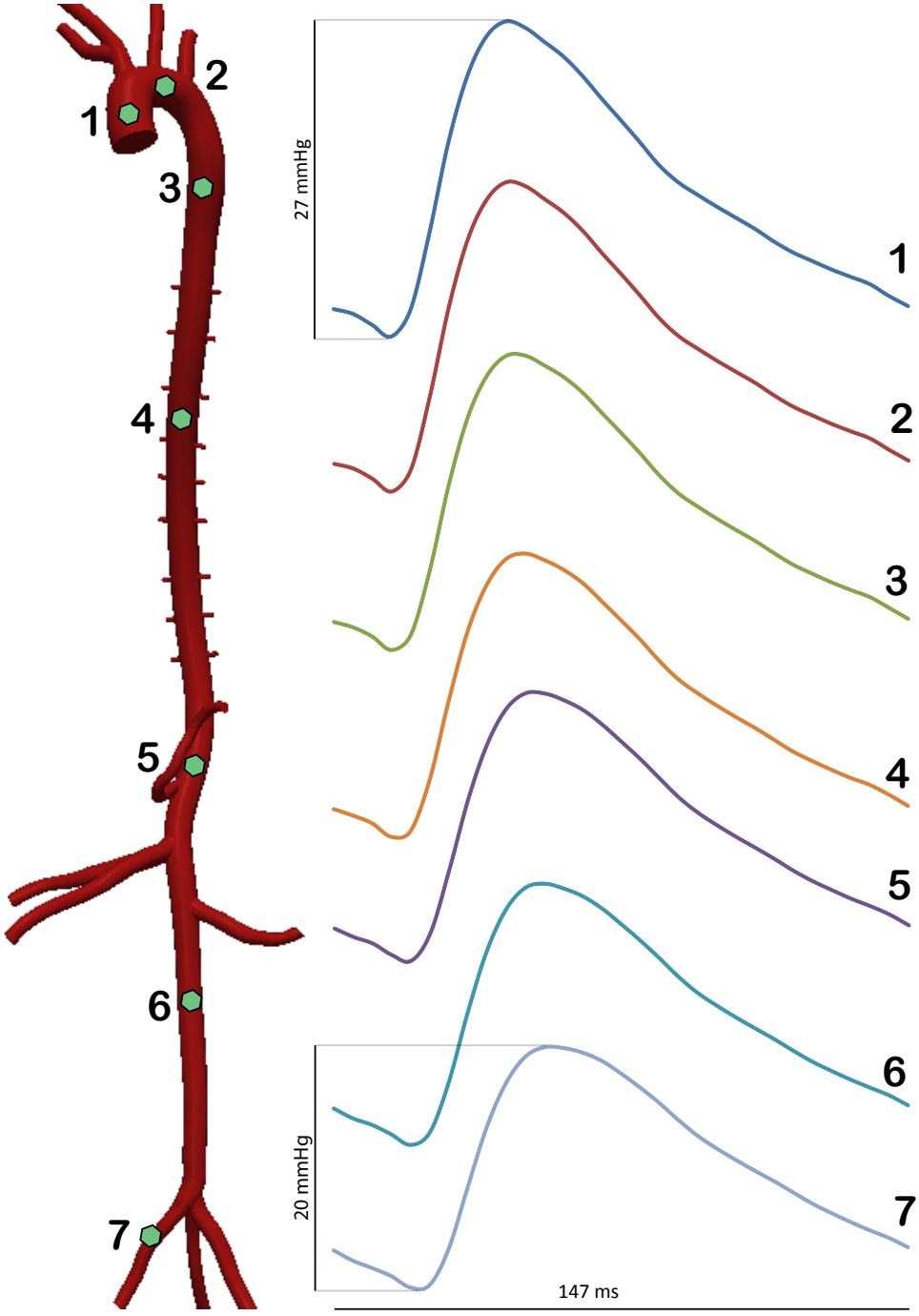

Figure 3.3: Pressure waveform at different locations in the aorta.

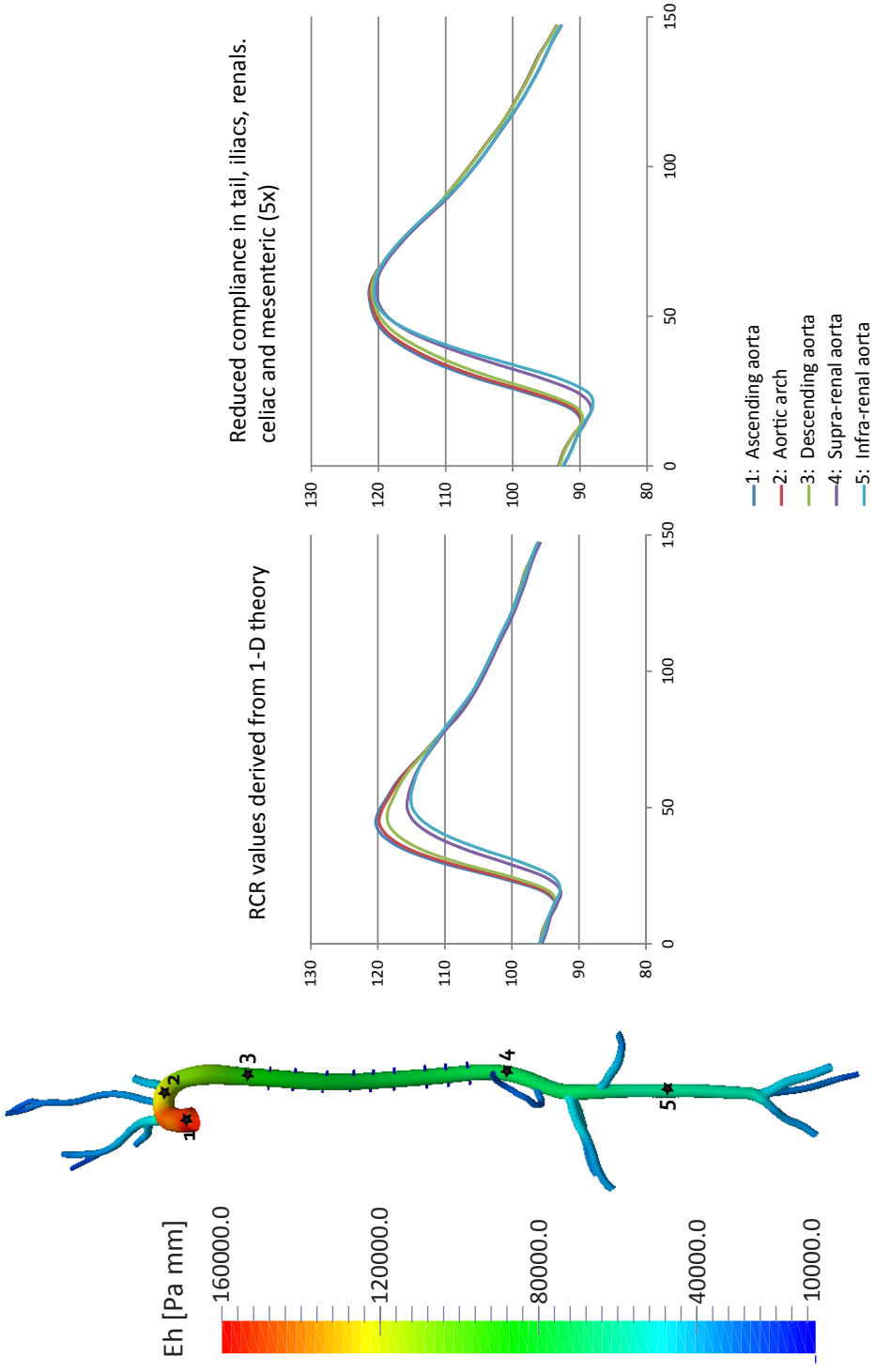

Figure 3.4: Pressure pulse propagation along the aorta for the baseline (left) and decreased peripheral compliance (right).

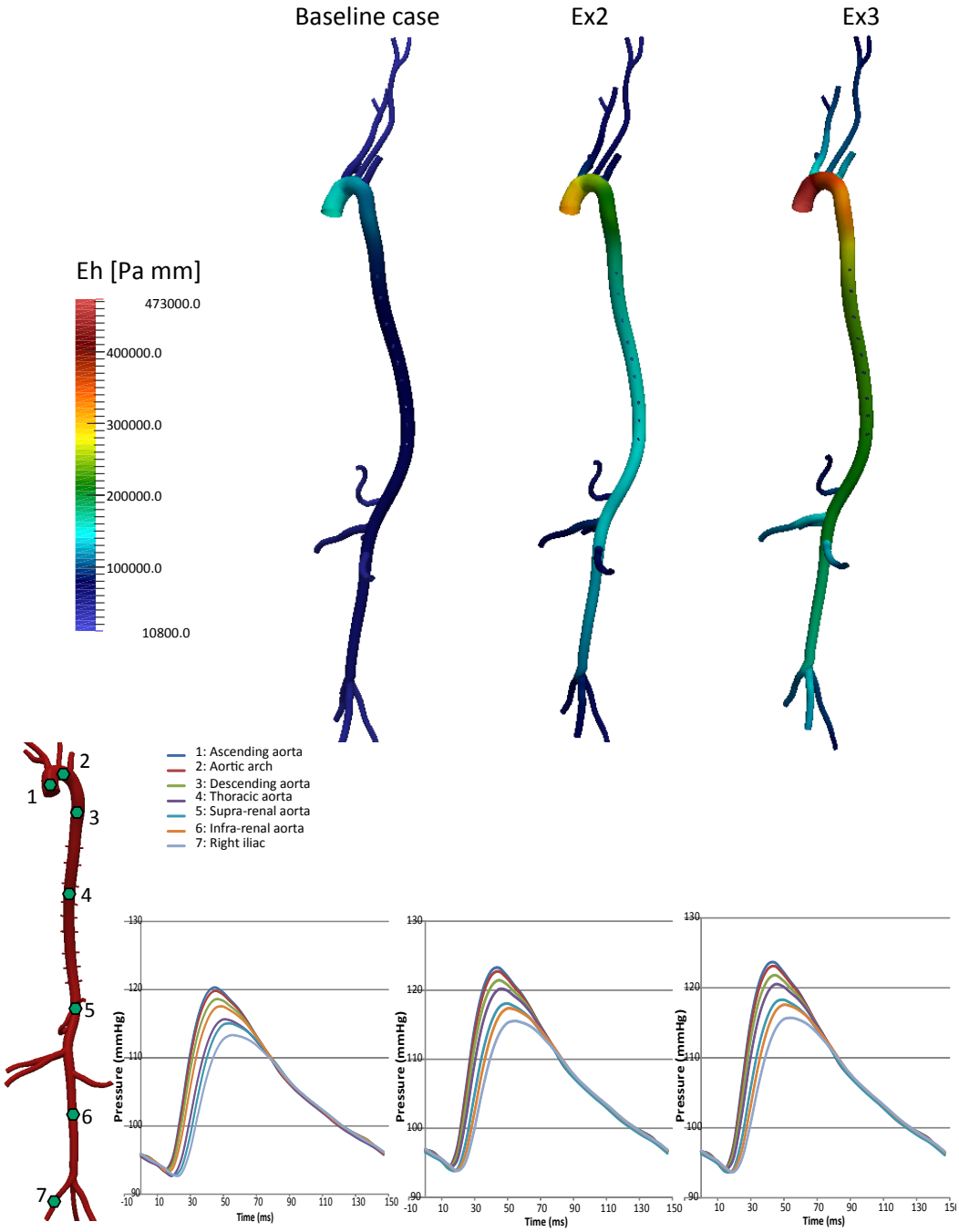

Figure 3.5: Pressure waveform in different location along the aorta in three different cases with increased levels of arterial stiffness.

Results show that pulse pressure increases with increasing stiffness. This is in agreement with experimental findings that report a significant difference in pulse pressure and systolic pressure between adult and old mice, but not in diastolic pressure [6].

Lastly, pulse wave velocity (PWV) values have been obtained by measuring the centerline distance between measurement sites and the time elapsed between the "feet" of the corresponding pressure waves (see Table 3.3). This is in good qualitative agreement with experimental measurements of wave speed; Reddy et al. [6] observed an increase of PWV in mice with aging. The measurement sites of the pressure used to calculate PWV are the aortic arch and infra-renal abdominal aorta, in order to be consistent with the reference.

	Baseline	Ex2	Ex3
PWV [cm/s]	696.7	864.87	964.66

Table 3.3: Pulse wave velocity (PWV) in three cases with increased stiffness.

Chapter 4

Discussion

In this thesis, an analysis of unsteady 3-D hemodynamics within a deformable arterial mouse model has been presented. The following methodologies have been used to pursue a physiologically realistic solution: a multi-domain method for outflow boundary condition specification, a coupled-momentum method for fluid structure interaction, an external tissue support boundary condition for representing perivascular support, and a method for a posteriori gradient-based mesh adaptation. A thorough literature search on geometrical data on the diameters of arterial system and hemodynamic data (flow and pressure waveforms) has been performed. Tissue properties have been provided by the department of Biomedical Engineering of Yale University. Using this information, four simulations were run: a baseline case, a simulation with modified Windkessel values representing reduced distal compliance and two simulations with increased aortic stiffness.

A good match between the average flow distribution and literature references was achieved (see Table 3.2). However the flow waveforms in left common carotid and innominate artery do not show the same shape as those reported by Feintuch et al. [3] (see Figure 4.1). A possible explanation for this mismatch could be the qualitative differences in the shape of the inflow used in the simulation and that recorded in the ascending aorta by Feintuch et al. [3] (see Figure 4.1). The latter presents a secondary peak in systole and backflow in diastole. In addition to these differences in inflow waveform,

the outflow RCR parameters could be further adjusted to achieve the desired flow waveforms.

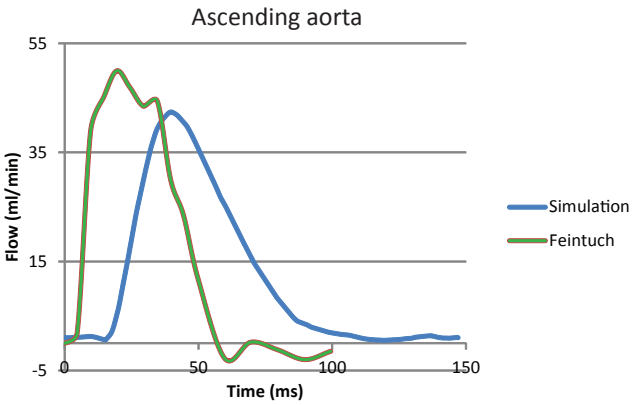

Figure 4.1: Cross sectional flow waveform in the ascending aorta: the data from Feintuch shows diastolic back flow.

Furthermore, the contour of the flow wave in the ascending aorta is greatly determined by the pattern of left ventricular ejection. In future work a lumped-parameter heart model will be used to simulate and couple the left ventricle and the arterial network, rather than prescribing a flow waveform.‘

The pressure waveforms in the ascending aorta are different in mice and young humans. In mice the pressure rises to a late systolic peak and then it falls after the incisura in an almost exponential manner, Without the secondary diastolic waves usually observable in humans [34]. Our simulated pressure waveforms are in good agreement with this observation. Another difference in the pressure waveforms of mice and humans is the lack of pulse pressure amplification in mice: indeed the pressure waves in the thoracic and the abdominal aorta showed similar amplitude as pressure in the ascending aorta [1]. We investigated the possibility of obtaining pressure amplification by iteratively reducing the compliance of peripheral vessels.

The two simulations with augmented aortic stiffness represent age-relating changes of vessel mechanical properties reported by Goyal [17]. Reddy et al. [6] showed augmentation of PWV and pulse pressure in old mice of 29

months old compared to adult mice of 8 months old. The increase of PWV with augmented stiffness is consistent with the Moens-Korteweg equation which asserts that PWV is proportional to square root of young modulus E:

$$PWV = \sqrt{\frac{Eh}{2r\rho}}$$

Increasing vessel stiffness and decreasing compliance values of the Windkessel model are two aspects of the same matter. Both contribute to decrease the total compliance of the system and therefore to increase the pulse pressure. However, this increase in pulse pressure is different in the two cases. Indeed, decreasing the peripheral compliances results in pressure waveforms exhibiting the same value in systole and lower diastolic values with increasing distance from the ascending aorta. Therefore the augmentation of pulse pressure is not spatially uniform. On the other hand, the case with increased stiffness shows similar diastolic values and larger and larger systolic values.

An important limitation of this thesis is the uncertainty and the multiple origins of the data utilized. A 3-D geometric model which does not exactly correspond to the actual dimensions of a mice is a factor that could strongly affect the results. The original 3-D geometry represented the qualitative shape (branching patterns and vessel length) of the arterial tree but with incorrect diameter dimensions; for this reason big part of the work consisted in obtaining representative data in literature on vessel diameters. The scaling of the original geometry was chosen to match the diameter average of each vessel with the values reported in literature. The same uncertainty applies to pressure. Pressure data in different locations were reported in different papers; and even though mouse strain, age and weight could be comparable, the experimental conditions are always different. This complicates the validation of pressure distributions in the simulations. Lastly, the tissue properties were only known at four different locations, and had to be interpolated to the entire model. Future work will involve considering the full biaxial data rather than just the circumferential component.

The real innovations of this work are the reproduction of physiological pressure waveforms and flow distribution in a realistic model of the mouse

vasculature.

Bibliography

[1] M. F. O. W W Nichols, "Mcdonald's blood flow in arteries. theoretical, experimental and clinical principles," vol. Fourth edition, 1998.

[2] H. L. Lujan and S. E. Dicarlo, "Cardiac output, at rest and during exercise, before and during myocardial ischemia, reperfusion, and infarction in conscious mice." *American journal of physiology. Regulatory, integrative and comparative physiology*, vol. 304, no. 4, pp. R286–95, Feb. 2013.

[3] A. Feintuch, P. Ruengsakulrach, A. Lin, J. Zhang, Y.-Q. Zhou, J. Bishop, L. Davidson, D. Courtman, F. S. Foster, D. a. Steinman, R. M. Henkelman, and C. R. Ethier, "Hemodynamics in the mouse aortic arch as assessed by MRI, ultrasound, and numerical modeling." *American journal of physiology. Heart and circulatory physiology*, vol. 292, no. 2, pp. H884–92, Feb. 2007.

[4] J. M. Greve, A. S. Les, B. T. Tang, M. T. Draney Blomme, N. M. Wilson, R. L. Dalman, N. J. Pelc, and C. a. Taylor, "Allometric scaling of wall shear stress from mice to humans: quantification using cine phase-contrast MRI and computational fluid dynamics." *American journal of physiology. Heart and circulatory physiology*, vol. 291, no. 4, pp. H1700–8, Oct. 2006.

[5] a. K. Reddy, G. E. Taffet, J. F. Prchal, L. H. Michael, M. L. Entman, and C. J. Hartley, "Effect of cellular elements on pressure-velocity relationship in mice." *Conference proceedings : ... Annual International Conference of the IEEE Engineering in Medicine and Biology Society.*

IEEE Engineering in Medicine and Biology Society. Conference, vol. 5, pp. 3720–2, Jan. 2004.

[6] A. K. Reddy, Y.-H. Li, T. T. Pham, L. N. Ochoa, M. T. Trevino, C. J. Hartley, L. H. Michael, M. L. Entman, and G. E. Taffet, "Measurement of aortic input impedance in mice: effects of age on aortic stiffness." *American journal of physiology. Heart and circulatory physiology*, vol. 285, no. 4, pp. H1464–70, Oct. 2003.

[7] B. N. Van Vliet, L. L. Chafe, and J.-P. Montani, "Characteristics of 24 h telemetered blood pressure in eNOS-knockout and C57Bl/6J control mice." *The Journal of physiology*, vol. 549, no. Pt 1, pp. 313–25, May 2003.

[8] J. J. McGuire, B. N. Van Vliet, and S. J. Halfyard, "Blood pressures, heart rate and locomotor activity during salt loading and angiotensin II infusion in protease-activated receptor 2 (PAR2) knockout mice." *BMC physiology*, vol. 8, p. 20, Jan. 2008.

[9] B. Vandeghinste, B. Trachet, M. Renard, C. Casteleyn, S. Staelens, B. Loeys, P. Segers, and S. Vandenberghe, "Replacing vascular corrosion casting by in vivo micro-CT imaging for building 3D cardiovascular models in mice." *Molecular imaging and biology : MIB : the official publication of the Academy of Molecular Imaging*, vol. 13, no. 1, pp. 78–86, Feb. 2011.

[10] C. Casteleyn, B. Trachet, D. Van Loo, D. G. H. Devos, W. Van den Broeck, P. Simoens, and P. Cornillie, "Validation of the murine aortic arch as a model to study human vascular diseases." *Journal of anatomy*, vol. 216, no. 5, pp. 563–71, May 2010.

[11] R. B. Hinton, C. M. Alfieri, S. a. Witt, B. J. Glascock, P. R. Khoury, D. W. Benson, and K. E. Yutzey, "Mouse heart valve structure and function: echocardiographic and morphometric analyses from the fetus through the aged adult." *American journal of physiology. Heart and circulatory physiology*, vol. 294, no. 6, pp. H2480–8, Jun. 2008.

[12] W. Wan, H. Yanagisawa, and R. L. Gleason, "Biomechanical and microstructural properties of common carotid arteries from fibulin-5 null mice." *Annals of biomedical engineering*, vol. 38, no. 12, pp. 3605–17, Dec. 2010.

[13] B. Trachet, M. Renard, G. De Santis, S. Staelens, J. De Backer, L. Antiga, B. Loeys, and P. Segers, "An integrated framework to quantitatively link mouse-specific hemodynamics to aneurysm formation in angiotensin II-infused ApoE -/- mice." *Annals of biomedical engineering*, vol. 39, no. 9, pp. 2430–44, Sep. 2011.

[14] X. Guo, Y. Kono, R. Mattrey, and G. S. Kassab, "Morphometry and strain distribution of the C57BL/6 mouse aorta." *American journal of physiology. Heart and circulatory physiology*, vol. 283, no. 5, pp. H1829–37, Nov. 2002.

[15] N. Xiao, J. Alastruey, and C. A. Figueroa, "A Systematic Comparison between 1-D and 3-D Hemodynamics in Compliant Arterial Models," pp. 1–22, 2012.

[16] C. A. Figueroa, I. E. Vignon-Clementel, K. E. Jansen, T. J. Hughes, and C. a. Taylor, "A coupled momentum method for modeling blood flow in three-dimensional deformable arteries," *Computer Methods in Applied Mechanics and Engineering*, vol. 195, no. 41-43, pp. 5685–5706, Aug. 2006.

[17] "Change with age in the aorta of man and mouse," *Experimenral gerontology*, vol. 17, pp. 127–132, 1982.

[18] "European cardiouvascular disease statistics," 2012.

[19] V. M. Barodka, B. L. Joshi, D. E. Berkowitz, C. W. Hogue, and D. Nyhan, "Implications of Vascular Aging," vol. 112, no. 5, pp. 1048–1060, 2011.

[20] A. Redheuil, W.-c. Yu, C. O. Wu, E. Mousseaux, A. D. Cesare, N. Kachenoura, D. Bluemke, J. A. C. Lima, and R. Yan, "Reduced

Ascending Aortic Strain and Distensibility Earliest Manifestations of Vascular Aging in Humans," pp. 319–326, 2010.

[21] J. S. Wilson, S. Baek, and J. D. Humphrey, "Importance of initial aortic properties on the evolving regional anisotropy, stiffness and wall thickness of human abdominal aortic aneurysms." *Journal of the Royal Society, Interface / the Royal Society*, vol. 9, no. 74, pp. 2047–58, Sep. 2012.

[22] E. G. Lakatta, M. Wang, and S. S. Najjar.

[23] N. Xiao, J. D. Humphrey, and C. A. Figueroa, "Author ' s personal copy Multi-scale computational model of three-dimensional hemodynamics within a deformable full-body arterial network," vol. 244, pp. 22–40, 2013.

[24] Y. Huo, X. Guo, and G. S. Kassab, "The flow field along the entire length of mouse aorta and primary branches." *Annals of biomedical engineering*, vol. 36, no. 5, pp. 685–99, May 2008.

[25] I. E. Vignon and C. a. Taylor, "Outflow boundary conditions for one-dimensional finite element modeling of blood flow and pressure waves in arteries," *Wave Motion*, vol. 39, no. 4, pp. 361–374, Apr. 2004.

[26] I. E. Vignon-Clementel, C. a. Figueroa, K. E. Jansen, and C. a. Taylor, "Outflow boundary conditions for 3D simulations of non-periodic blood flow and pressure fields in deformable arteries." *Computer methods in biomechanics and biomedical engineering*, vol. 13, no. 5, pp. 625–40, Oct. 2010.

[27] C. Tsukahara, F. Sugiyama, B. Paigen, S. Kunita, and K.-I. Yagami, "Blood pressure in 15 inbred mouse strains and its lack of relation with obesity and insulin resistance in the progeny of an NZO/HILtJ x C3H/HeJ intercross." *Mammalian genome : official journal of the International Mammalian Genome Society*, vol. 15, no. 12, pp. 943–50, Dec. 2004.

[28] J. N. Lorenz and E. G. Kranias, "Regulatory effects of phospholamban on cardiac function in intact mice Regulatory effects of phospholamban on cardiac function in intact mice," 2013.

[29] I. Giuvărăşteanu, "Scanning electron microscopy of vascular corrosion casts–standard method for studying microvessels." *Romanian journal of morphology and embryology = Revue roumaine de morphologie et embryologie*, vol. 48, no. 3, pp. 257–61, Jan. 2007.

[30] U. Wr, E. Sdwlhqw, V. Jhrphwulf, P. Iurp, P. Lpdjlqj, and G. Iurp, "* HRPHWULF 0RGHOV IURP 0HGLFDO , PDJLQJ ' DWD IRU."

[31] I. E. Vignon-Clementel, C. Alberto Figueroa, K. E. Jansen, and C. a. Taylor, "Outflow boundary conditions for three-dimensional finite element modeling of blood flow and pressure in arteries," *Computer Methods in Applied Mechanics and Engineering*, vol. 195, no. 29-32, pp. 3776–3796, Jun. 2006.

[32] P. Moireau, N. Xiao, M. Astorino, C. a. Figueroa, D. Chapelle, C. a. Taylor, and J.-F. Gerbeau, "External tissue support and fluid-structure simulation in blood flows." *Biomechanics and modeling in mechanobiology*, vol. 11, no. 1-2, pp. 1–18, Jan. 2012.

[33] P. Reymond, F. Merenda, F. Perren, D. Rüfenacht, and N. Stergiopulos, "Validation of a one-dimensional model of the systemic arterial tree." *American journal of physiology. Heart and circulatory physiology*, vol. 297, no. 1, pp. H208–22, Jul. 2009.

[34] W. F. Hamilton and R. A. Woodbury, "THE AMERICAN OF PHYSIOLOGY," vol. 119, 1937.